Lattice Dynamics in the $SnSb_2Te_4$ Phase Change Material

von

Jens Gallus

Diplomarbeit in Physik

vorgelegt der

Fakultät für Mathematik, Informatik und Naturwissenschaften

der Rheinisch-Westfälischen Technischen Hochschule Aachen

im
Oktober 2011

angefertigt am

Jülich Centre for Neutron Science JCNS und Peter Grünberg Institut PGI - Streumethoden, Forschungszentrum Jülich

Prof. Dr. Matthias Wuttig, RWTH Aachen

Dr. Raphaël Hermann, Inv. Prof., Université de Liège

Ich versichere, dass ich die Arbeit selbstständig verfasst und keine anderen als die angegebenen Quellen und Hilfsmittel benutzt, sowie Zitate kenntlich gemacht habe.

Aachen, den 14. Oktober 2011

Contents

Chapter 1

Introduction

Phase Change Materials (PCMs) are promising candidates for a new generation of data storage as they combine both the advantage of non-volatile data storage and high speed memory transfer. They are characterized by outstanding optical and electronic property contrasts and a fast switching between an amorphous and at least one crystalline phase [1]. In order to switch from the amorphous to the crystalline state the material is heated above its crystallization temperature. The opposite direction is accessible by heating above the melting temperature and subsequent rapid quenching ($> 10^9$ K/s) into the disordered amorphous phase.

At the beginning of the 1990s the application of rewritable optical data storage was discovered for Ag-In-Sb-Te and Ge-Sb-Te alloys. The compounds $GeSb_2Te_4$ and $Ge_2Sb_2Te_5$ were the most common representatives due to their long-term stability at ambient temperatures and their fast switching (50 ns) between the amorphous and the crystalline phase (NaCl structure) [1]. Nowadays, these PCMs are applied for DVDs and Blu-Ray disks by utilizing the significant difference in optical reflectivity between the amorphous and the crystalline phase which increases for about 30% upon crystallization [2]. Another large property contrast can be observed in the electrical resistivity which drops for several orders of magnitude in the ordered crystalline structure. This large difference could be the basis for a new kind of non-volatile random access memories (RAMs).

The applicability of PCMs is strongly dependent on the stoichiometry. Figure 1.1 shows a ternary phase diagram depicting different phase change alloys including their form and initial year of application [3]. The most important area is the pseudo binary line which extends between GeTe and Sb_2Te_3 including alloys such as $GeSb_2Te_4$ and $Ge_2Sb_2Te_5$. The materials of this area are most studied PCMs characterized by a very low crystallization time and a pronounced property contrast between the amorphous and the crystalline phase.

As there is no straightforward way to find new PCMs, Littlewood [4, 5], for example, developed a diagram for binary compounds introducing two coordinates which were called "ionicity" and "covalency" (or "hybridization"). The first coordinate is comparable to the electronegativity
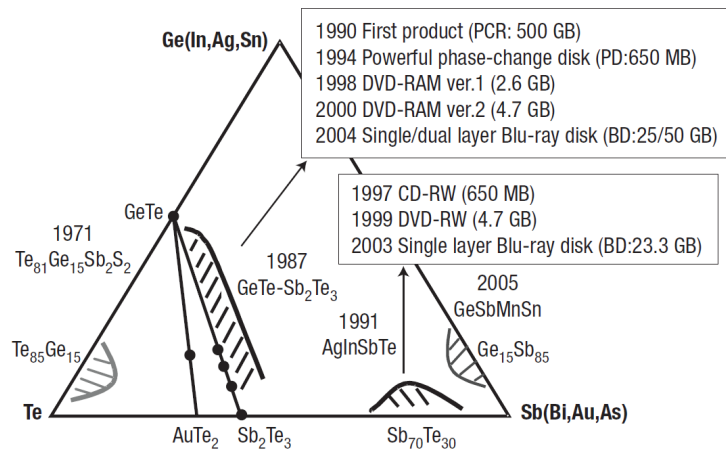
Figure 1.1: *Ternary phase change diagram for Te, Sb and Ge [3]. The area between GeTe and Sb_2Te_3 (pseudo binary line) provides many useful PCMs characterized by a large property contrast between the amorphous and the crystalline phase and by low crystallization times.*

difference and the latter can be understood as a value for the energetic splitting of the electronic s- and p-states. In 2008 Lencer et al. [6] enhanced this diagram to ternary compounds including more suitable PCMs. In this "treasure map" they modified the previous concept by separating the three compounds into cations and anions and thus substitute the material by an equivalent binary compound. The result is shown in Figure 1.2. In this map all well-known PCMs are located in the same small region defined by an upper limit of ionicity and hybridization. Thus this treasure map suggests a limiting region to the number of PCMs and offers criteria to identify suitable PCMs.

A first step in order to explain both the large property contrast between the two phases in PCMs as well as the low increase of thermal conductivity upon crystallization was achieved by suggesting two different kinds of bonds [7] dependent on the phase. In the amorphous state an ordinary covalent bonding occurs which leads to localized electrons and a large force constant. Upon switching to the crystalline phase, however, a change to another type of bonding occurs which has been called "resonant bonding" (see Figure 1.3). In this very special type of bonding six near neighbours have to share three p-electrons on average which leads to a collective shifting of electrons between the atoms and forming locally covalent bondings. The appearance of delocalized electrons causes a large increase in reflectivity exploited in optical data storages.

This diploma thesis deals with the compound $SnSb_2Te_4$. The target of this thesis is to improve the knowledge of the lattice dynamics with respect to the low thermal conductivity and the large anharmonicity of the crystalline phase of PCMs and to verify the picture obtained in former studies. From nuclear inelastic scattering experiments an elastic hardening of low energy modes as well as a vibrational softening was observed for the isotopes Sb and Te in GST. However, the

Figure 1.2: *Treasure map created by Lencer et al. [6] for PCMs consisting of ternary or quaternary compounds. The bottom figure shows a magnified area which includes the currently most successful PCMs.*

density of phonon states is not accessible for Ge. In $SnSb_2Te_4$ an isoelectronic substitution of Ge by Sn is made providing the possibility to measure all three isotopes for the amorphous and two crystalline phases. The information about Sn can be used to gain information about Ge and whether Ge shows the same characteristics as Sb and Te.

The second chapter of this thesis provides the theoretical background as a basis for the principle of PCMs and the following measurements. Chapter 3 deals with the preparation of the samples which was performed both via vapour deposition and magnetron sputtering. Characterization methods are presented in the fourth chapter. X-ray diffraction, temperature dependent resistivity measurements and resonant ultrasound spectroscopy were used to determine characteristic parameters of $SnSb_2Te_4$ such as lattice constants, resistivity, and speed of sound.

Figure 1.3: *A schematic illustration of resonant bonding for a hypothetical simple cubic Sb crystal. On average six Sb atoms share three electrons. The outer pictures show two limiting cases with a shift of electron pairs between the atoms. In reality a superposition of these cases (central picture) is observed leading to a pronounced electron delocalization [7].*

The focus of this work lies on the method of nuclear inelastic scattering (NIS) presented in Chapter 5 which was utilized at the European Synchrotron Radiation Facility at beamlines ID22N and ID18. With this method one is able to extract the density of phonon states. As there are Mößbauer active isotopes for Sn, Sb and Te, the great advantage of $SnSb_2Te_4$ is that in this PCM the density of phonon states can be measured for all its components. NIS gives access to the lattice dynamics and to the microscopic change of the material upon phase transition. These results bring further knowledge about functionality of PCMs characterized by the change of the bonding type and give the opportunity to improve future applications.

Chapter 6 summarizes all relevant information, compares the results with the results from other PCMs and gives an outlook for next steps of characterization of PCMs.

Chapter 2

Theoretical Background

2.1 Properties of Phase Change Materials

Phase change materials (PCMs) are characterized by a high contrast in optical and structural properties between the amorphous and the crystalline state. The reflectivity increases by about 30 % depending on the material, while the resistivity decreases by several orders of magnitude. On the other hand there is no significant increase with respect to the thermal conductivity. The cubic phase of $Ge_2Sb_2Te_5$, for example, has a thermal conductivity of about 0.44 $WK^{-1}m^{-1}$ which is comparatively just slightly higher than for the amorphous phase with 0.25 $WK^{-1}m^{-1}$. Ordinary semiconductors such as Ge or GaAs exhibit a four to five times higher thermal conductivity in the crystalline phase as compared with the amorphous state [8].

Recently published data show a large temperature dependence both of the bond lengths as well as of the atomic displacement parameter in the crystalline phase which is not observed in the corresponding amorphous one [8]. This leads to the conclusion of large lattice distortions and to a large anharmonicity of the crystalline material. Figure 2.1 shows a schematic plot for the potential energy for both phases. The potential of the amorphous state has a parabolic shape whereas the potential for the metastable crystalline phase shows a large anharmonicity and, due to large distortions, more than one equilibrium state which can be occupied by the atoms.

2.1.1 Phase Transitions

Thermal stability and the occurrence of phase transitions is expressed by the free enthalpy (also called Gibbs energy) G of a system which is defined by the equation

$$G = U + pV - TS \tag{2.1}$$
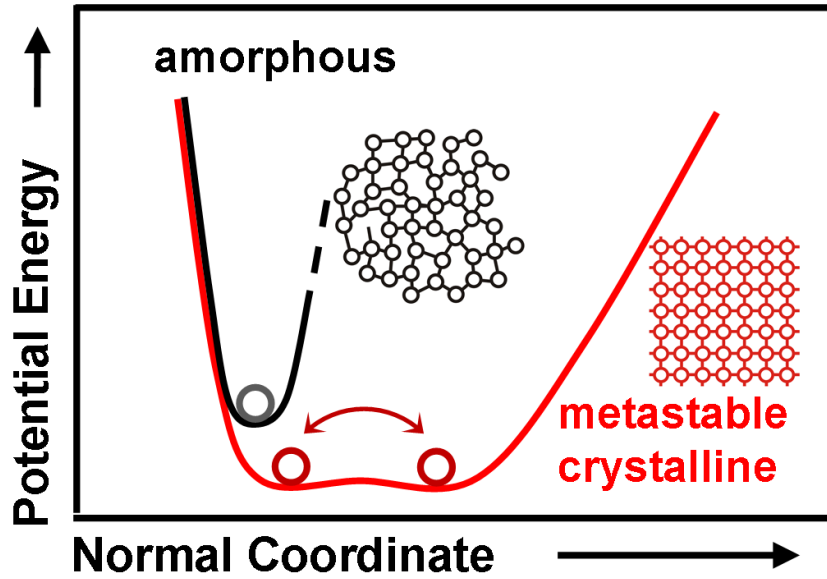
Figure 2.1: *Schematic illustration of the potential energies for the amorphous and the cubic phase of an arbitrary PCM. For the amorphous phase the potential is harmonic, however, the potential of the crystalline state exhibits large anharmonicity and more than one energy minimum [8].*

with the internal energy U, pressure p, volume V, temperature T and entropy S [9]. A thermodynamic equilibrium state is realised if the system is located in a global minimum of the free enthalpy, i.e.

$$\Delta G = 0 \tag{2.2}$$

In case the system is located in a local minimum, i. e. in a metastable state, the system can hop into the global minimum by crossing an activation potential. The quantity ΔG is also called "driving force" because it actuates the appearance of a phase transition. For example, the transition from the liquid l to the crystalline state c of a system, is determined by the difference of free enthalpies of both phases:

$$\Delta G = G_l - G_c \tag{2.3}$$

The temperature dependence of such a system is illustrated in Figure 2.2. At the melting temperature T_m the liquid and the crystalline phase coexist which means that the free enthalpy difference between these phases vanishes [3]. By cooling down the system ΔG constantly grows while the atomic mobility μ decreases with temperature. Close to the glass-transition temperature T_g the driving force of the formation of crystalline nuclei is large, however, atomic

mobilities are low. The fastest crystallization occurs at temperatures between T_m and T_g with a certain balance between mobility and driving force.
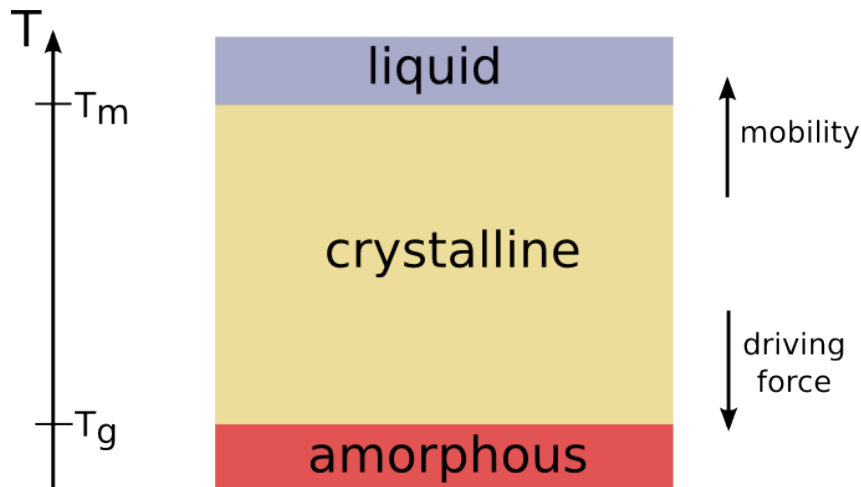
Figure 2.2: *Temperature dependence of a system with different structural phases. The driving force between the liquid and the crystalline phase below T_m increases with decreasing temperature. Simultaneously atomic mobilities decrease. The largest crystallization time appears at intermediate temperatures.*

Upon transition into the crystalline phase, an amorphous material forms a regular structure with a long range order. The crystallization process is divided into formation of nuclei and their subsequent growth. In an amorphous material the driving force actuates the atoms to form more stable crystallites and as soon as a critical amount is available, the growing process begins. For both procedures an activation potential has to be overcome which can be provided by the thermal energy.

Phase Change Materials (PCMs) can be switched reversibly between the amorphous and at least one crystalline phase. In Ge-Sb-Te compounds one metastable NaCl phase appears within a small temperature range before it passes into a stable hexagonal structure. In current applications the phase transition from amorphous to the cubic phase is exploited because of the low crystallization time (ns-range). Optical and thermodynamic properties of the two crystalline phases normally do not differ significantly but are observable.

A schematic illustration of the functionality of phase change materials is shown in Figure 2.3. A short high laser (a) or current (b) pulse (also called "reset pulse") heats the material above its melting temperature. Then the material cools down rapidly due to convection from the surrounding and remains in an amorphous phase similar to a frozen liquid. This "spot" can be understood as the logical "1" for the data storage. However, the quenching has to take place rapidly (cooling rate $> 10^8 \frac{\text{K}}{\text{s}}$). To switch back to the crystalline state a long and low intensity laser or current pulse is needed (also called "set pulse"). In this case the illuminated area is heated above the glass transition temperature and builds up a long range ordered NaCl-

structured phase which represents the logical "0". To read the single bits a laser or current of low intensity is applied to the material.
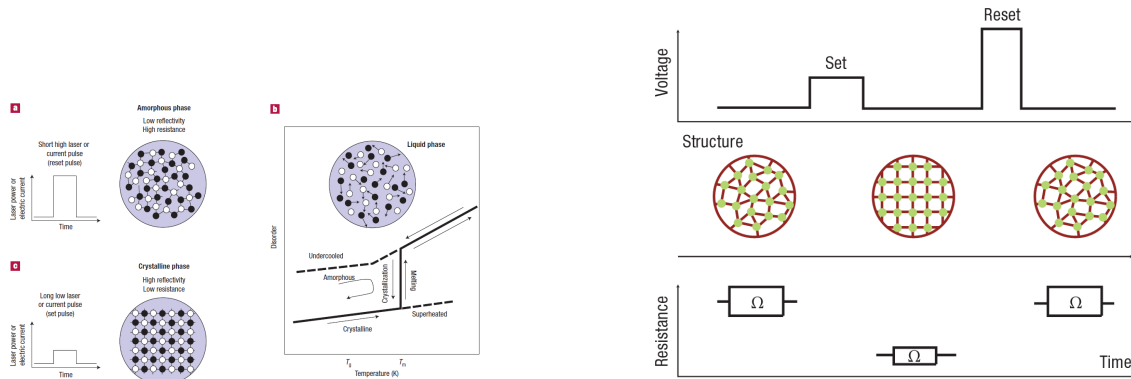
(a) The amorphous material is switched into the crystalline state via laser pulses as it is applied in optical data storages [3].

(b) Switching between the amorphous and crystalline state in phase change materials via electric pulses. Determining the phase is probed by measuring the resistivity [10].

Figure 2.3: *Schematic plot of switching between amorphous and crystalline state in phase change materials via laser or electronic pulses.*

2.1.2 Structural Properties of SnSb$_2$Te$_4$

This thesis is focused on the phase change material SnSb$_2$Te$_4$. This ternary alloy consists of three consecutive elements of the periodic table with all constituents having at least one Mößbauer active isotope ([119]Sn, [121]Sb, [125]Te). SnSb$_2$Te$_4$ is isoelectric to the most common PCMs GeSb$_2$Te$_4$ with the additional possibility to get access to the partial density of phonon states of all three elements (see Chapter 5).

SnSb$_2$Te$_4$ exists in the amorphous as well as one NaCl-type and one hexagonal structure. The unit cell for both crystalline phases is presented in Figure 2.4. The red, yellow and blue circles represent the Sn, Sb and Te atoms, respectively.

The cubic phase consists of two face centred sublattices with the space group $Fm\bar{3}m$. The Te atoms occupy one sublattice and the other sublattice is statistically filled up by one Sn- and two Sb Atoms. The mixed coloured circles indicate the occupation probability of the atomic positions, i.e. two of four of these positions are occupied by Sb atoms, one by a Sn atom and one remains vacant.

The unit cell of the stable hexagonal structure is more complex. The related space group is $R\bar{3}mH$ indicating a rhombohedral structure which can be represented by a hexagonal unit cell consisting of 21 atomic sequences perpendicular to the c-axis [11]. It can be separated into three seven-layer packages including four Te layers with two of them representing the the outer

(a) NaCl structure.

(b) Hexagonal structure.
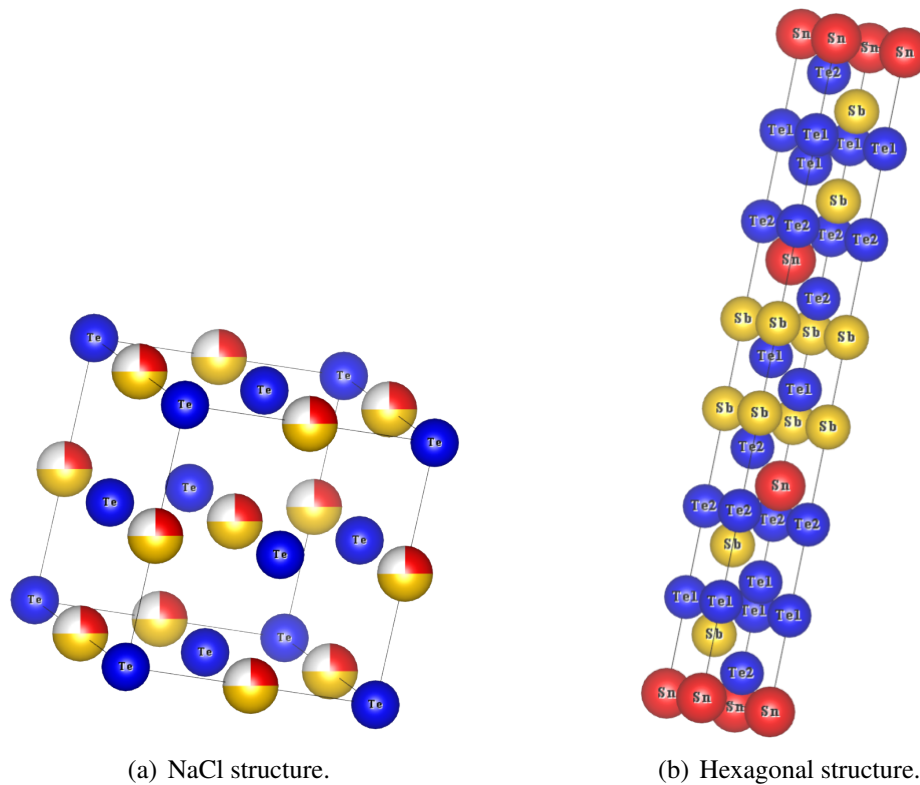
Figure 2.4: *Structures of the two crystalline phases of SnSb$_2$Te$_4$.*

layers of each package (indicated as Te1 in Figure 2.4). In this structure vacancy layers separate neighbouring packages which are weakly bonded by van der Waals interaction [12].

2.2 X-Rays

X-rays are electro-magnetic waves with energies between 100 eV and some MeV which correspond to wavelengths between 10^{-8} to 10^{-12} m. As these wavelengths lie in the range of the distance between atomic plains, x-ray experiments are performed to determine crystallographic structures.

2.2.1 X-Ray Sources

In general there are two ways to produce x-rays. The first possibility is the excitation of electrons to higher energy levels and their subsequent de-excitation accompanied by the emission of a photon in the x-ray energy range which is applied in x-ray tubes. If charged particles are accelerated, for example by magnetic fields, a continuous spectrum of electromagnetic radiation

is emitted, so called Bremsstrahlung. A special case of Bremsstrahlung is synchrotron radiation which is produced in large synchrotron radiation facilities.

X-ray Tube

An x-ray tube consists of an evacuated volume with a cathode and an anode (Figure 2.5) [13]. A high voltage (25-150 kV) between these electrodes causes a flow of electrons starting from the cathode towards the anode (usually copper or molybdenum). There the speed of the electrons is reduced by emitting Bremsstrahlung whose energy depends on the value of deceleration inside the material. Because of the high velocity of the electrons they may also reach the inner shells of the atoms and make one of the highly bounded electrons leave the atom. The resulting hole is filled by an electron of an outer shell emitting a photon with the characteristic energy for this transition. In contrast to the continuous bremsstrahlung, the energy of this kind of emission has a discrete spectrum.
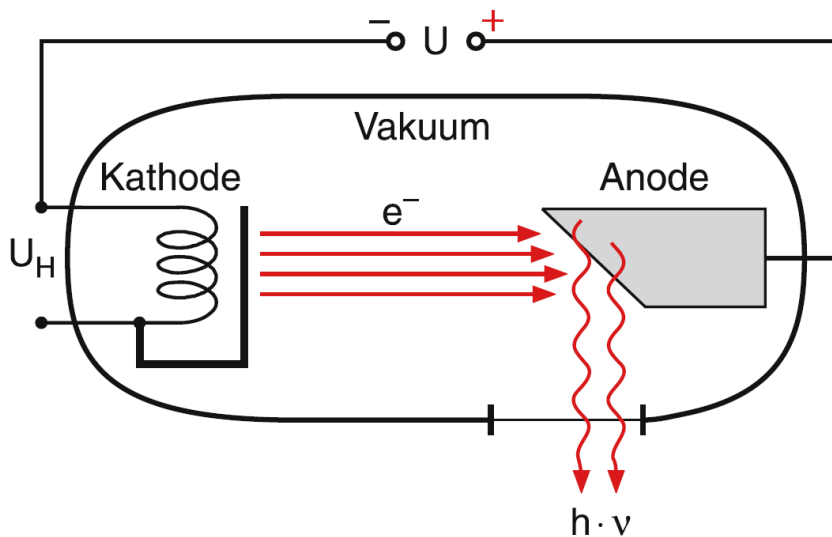
Figure 2.5: *Schematic plot of an x-ray tube [13].*

Synchrotron Radiation

Synchrotron radiation is the general expression for the radiation emitted tangentially by accelerated, charged particles [14]. In a synchrotron radiation source this effect is applied by a magnetic field in order to create high energy x-rays. A synchrotron radiation facility consists of a large storage ring (e.g. circumference of the ESRF is 844 m, see Figure 2.6) in which electrons are accelerated near to the speed of light. In order to prevent collision of electrons with external particles, the storage ring is under high vacuum.

The high speed electrons are forced on orbits by bending magnets placed along the ring. The electrons are accelerated due to the Lorentz force and a wide spectrum of continuous x-rays is emitted. This radiation reveals a very high photon flux and highly collimated beams can be used to investigate small samples. In order to produce photons with sharply defined energies, insertion devices such as wigglers or undulators are installed. These devices consist of a consecutive construction of several dipole magnets in which the electrons are forced to sinusoidal trajectories [14].

The electrons of synchrotron radiation facilities are emitted from buckets in pulses of radiation with a time resolution ps range. This is a useful characteristic which makes time resolved inelastic nuclear scattering possible.

Figure 2.6: *The synchrotron ring of the ESRF, Grenoble, France.*

An additional characteristic of synchrotron radiation is its polarization which depends on the electrons' oscillation plane. In present synchrotron rings electrons are excited to sinusoidal oscillations in the plane of the ring, so that the emitted waves are polarized linearly with a horizontal oscillation of the electric field vector.

2.2.2 X-Ray Diffraction

X-rays are diffracted by the electron clouds around atoms. At a sufficiently large distance from the source the incident wave may be described by a plain wave (Fraunhofer approximation) with the wave vector $\vec{k}$ and the scattered wave is described by $\vec{k'}$. The difference between these quantities is defined as the scattering vector [15].

$$\vec{Q} = \vec{k'} - \vec{k}. \tag{2.4}$$

In the case of an elastic process one can assume

$$|\vec{k}| = |\vec{k'}| = \frac{2\pi}{\lambda} \tag{2.5}$$

with the wavelength λ. The absolute modulus of the scattering vector is given by:

$$|\vec{Q}| = \sqrt{|\vec{k}|^2 + |\vec{k'}|^2 - 2|\vec{k}||\vec{k'}|cos(2\theta)} = \frac{4\pi}{\lambda}sin(\theta). \tag{2.6}$$

where 2θ is the angle included by the incident and the emitted wave (Figure 2.7).
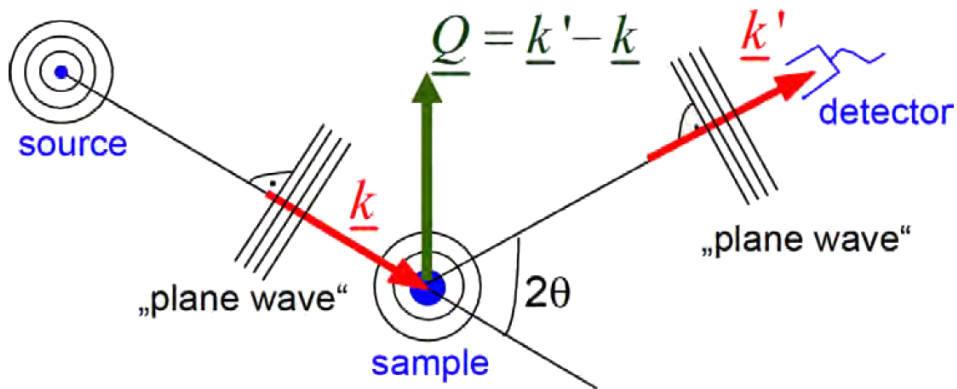
Figure 2.7: *Fraunhofer approximation and the scattering vector [15].*

In a periodic structure, diffracted waves of the same phase interfere constructively. This is exactly the case if the scattering vector equals a reciprocal lattice vector $\vec{G}$ of the crystal:

$$\vec{Q} = \vec{G} \tag{2.7}$$

The latter equation is also called "Laue condition". An equivalent description is given by the Bragg's law:

$$n\lambda = 2dsin\theta \tag{2.8}$$

In this equation the right hand-side shows the path difference between two diffracted waves with the distance d between two lattice planes and the scattered angle θ. If this path difference is equal to an integer factor of the incoming wavelength λ, constructive interference occurs (Figure 2.8).

For a cubic structure the lattice distance d can be expressed by the Miller indices h, k and l:
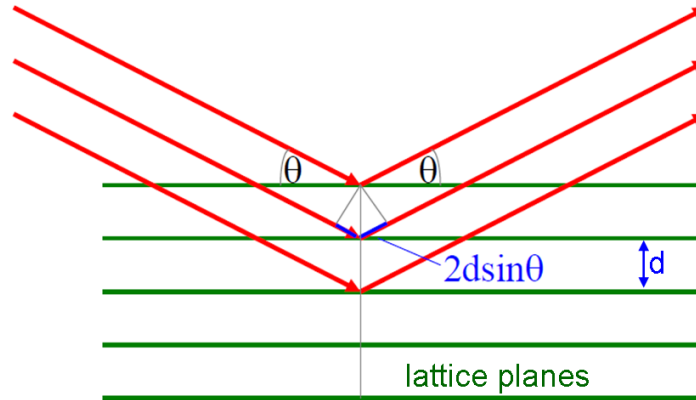
Figure 2.8: *The Bragg equation illustrated for a wave scattered at several lattice planes [15].*

$$d = \frac{a}{\sqrt{h^2 + k^2 + l^2}} \tag{2.9}$$

By measuring the angle of the diffracted waves with respect to the direction of the direct beam one is able to determine the lattice parameter a assuming that the single peaks can be identified with the Miller indices.

The scattered amplitude A at the position $\vec{r}$ of a wave is dependent on the scattering density ρ at that point [15]:

$$A = A_0 \int \rho(\vec{r}) e^{i\vec{Q}\vec{r}} dV \tag{2.10}$$

In the latter equation A_0 denotes the amplitude of the incident wave. The scattered amplitude is connected to the scattering density by a Fourier transformation. The measurable quantity at scattering experiments is the intensity of the scattered waves. It is calculated by the square modulus of the amplitude:

$$I = |A|^2 = A \cdot A^* \tag{2.11}$$

However, because of the square modulus the phase information is lost so that the reconstruction of the scattering density is impossible. This is known as the "phase problem" of scattering.

2.3 Phonons

Phonons are the quanta of lattice waves with momentum $\vec{p} = \hbar\vec{k}$ and energy $E = \hbar\omega$. In the harmonic and adiabatic approximation, they are represented by harmonic oscillators with the energy Eigenvalues [16]

$$E = (n + \frac{1}{2})\hbar\omega. \tag{2.12}$$

with the main quantum number n and frequency ω.

Creation or annihilation of phonons by scattering of particles such as photons or neutrons can be described using inelastic processes. In these processes the frequency of the incident particle is shifted by the frequency of the contributing phonon which is described by the following equations:

$$\hbar\omega = \hbar\omega_0 \pm \hbar\omega \tag{2.13}$$

$$\hbar\vec{k}' - \hbar\vec{k} \pm \hbar\vec{Q} = \hbar\vec{G} \tag{2.14}$$

The first equation describes the energy conservation of the process. The transition energy $\hbar\omega$ consists of the energy of the incoming particle $\hbar\omega_0$ and the energy of the absorbed or emitted phonon. The second equation is considered as quasi-momentum conservation which is defined by one single reciprocal lattice vector $\vec{G}$. The additional term $\hbar\vec{Q}$ represents the quasi-momentum of the phonon.

Phonons can be separated into acoustic and optical phonons. Acoustic phonons are due to atoms that move in phase, and they significantly contribute to the propagation of thermal waves in a solid. Optical phonons are caused by out of phase oscillations. Their name comes from the opposite movement of differently charged ions in a crystal leading to a dipole moment which is active to e.g. infrared light. A crystal consisting of r atoms in the primitive unit cell has $3r$ phonon modes which are separated into 3 acoustic (1 longitudinal, 2 transversal) and $3r$-3 optical modes (r-1 longitudinal, $2r$-2 transversal).

In a solid a heat flow $\vec{Q}$ is related to a temperature gradient $\vec{\nabla}(T)$ by the Fourier law:

$$\vec{Q} = -\lambda\vec{\nabla}(T) \tag{2.15}$$

In the latter equation λ represents the coefficient of thermal conductivity. Thermal conduction can be divided into the contribution of the lattice and of free electrons:

$$\lambda = \lambda_{lattice} + \lambda_{electrons} \tag{2.16}$$

In case the electronic contribution to the thermal conductivity is negligible, a heat flow only occurs if the number of phonons between two different positions differs from the equilibrium value. With the Ansatz that a temporal variation of the number of phonons can be caused by propagation and scattering of phonons, the thermal coefficient is described as:

$$\lambda = \frac{1}{3V} \sum_{\vec{q},j} v(\vec{q},j) \Lambda(\vec{q},j) \frac{\partial}{\partial T} \epsilon(\omega(\vec{q},j), T). \tag{2.17}$$

In the above approximation the thermal coefficient depends on the wave velocity v, the mean free path $\Lambda = v\tau$ and the mean energy of the phonons which is given by

$$\epsilon(\omega(\vec{q},j), T) = \hbar\,\omega\left(\frac{1}{2} + \frac{1}{e^{\frac{\hbar\omega}{k_B T}} - 1}\right) \tag{2.18}$$

2.4 Density of States and Debye Approximation

The density of states (DOS) $g(\omega)$ describes the number of states in an infinitesimal energy or frequency interval [16]:

$$g(\omega)d\omega = \frac{V}{(2\pi)^3} \int_{\omega}^{\omega+d\omega} d\vec{q}. \tag{2.19}$$

It is dependent on the slope $\frac{\partial q}{\partial \omega}$ of the dispersion relation $\omega(\vec{q})$, i.e. the more flat the dispersion, the more states are occupied in this interval. In case the mode is flat, the DOS exhibits a singularity, a so called van Hove singularity.

In the Debye approximation vibrations in a solid are modelled as harmonic oscillators vibrating with different frequencies up to a limiting frequency which is called Debye frequency. The Debye frequency is also connected to the Debye energy or the Debye temperature. Debye energy or Debye temperature. By assuming linear dispersion relation, for an elastic, isotropic medium with longitudinal c_l and transversal sound velocity v_t, the density of states is then calculated from

$$g(\omega)d\omega = \frac{V}{2\pi^2}\left(\frac{1}{v_l^3} + \frac{2}{v_t^3}\right)\omega^2 d\omega. \tag{2.20}$$

The latter equation indicates that the DOS increases quadratically with ω for small frequencies.

2.5 Mößbauer Effect

The Mößbauer effect is named after the German physicist Rudolf Mößbauer who received the Nobel price for his discovery in 1962. It describes the recoilless emission or absorption of gamma rays by atomic nuclei bound in a solid.

If a free nucleus returns from an excited state E_e to the ground state E_g by emitting a photon, it experiences a recoil momentum [17]:

$$Mv_x \; = \; \frac{E_\gamma}{c} \; + \; M(v_x \, - \, v_R) \tag{2.21}$$

The initial momentum in x-direction Mv_x of the nucleus with mass M is decreased by a recoil momentum Mv_R caused by the emitted photon with energy E_γ. The energy conservation for this process leads to:

$$E_e + \frac{1}{2}Mv_x^2 = E_g + E_\gamma + \frac{1}{2}M(v_x - v_R)^2 \tag{2.22}$$

Solving this equation with respect to E_γ:

$$E_\gamma = (E_e - E_g) - \frac{1}{2}Mv_R^2 + Mv_x v_R = E_0 - E_R + E_D \tag{2.23}$$

E_0 is defined as the energy difference between the excited and the ground state while E_R represents the recoil energy of the nucleus. The quantity E_D is known as the Doppler energy shift and depends on the initial velocity of the nucleus v_x. If $v_x = 0$, the Doppler shift equals zero, thus the energy of the emitted photon has a sharp peak at the energy E_0 - E_R whose broadening is just determined by the natural lifetime of the nucleus. The equivalent energy for an absorbed photon is shifted by the recoil energy E_R to larger energies, so that the energy difference between emitted and absorbed photon amounts $2E_R$. This circumstance is illustrated by the sharp peaks in Figure 2.9. The wide solid lines show the case for $v_x \neq 0$ which leads to a large Doppler broadening of the energy peaks.

If the nucleus is now placed inside a crystalline lattice, it proceeds oscillations along its equilibrium state which can be interpreted as lattice waves or phonons. Such a quantum with frequency ω can only transfer energies in integer multiples of $\hbar\omega$. Thus there is a probability
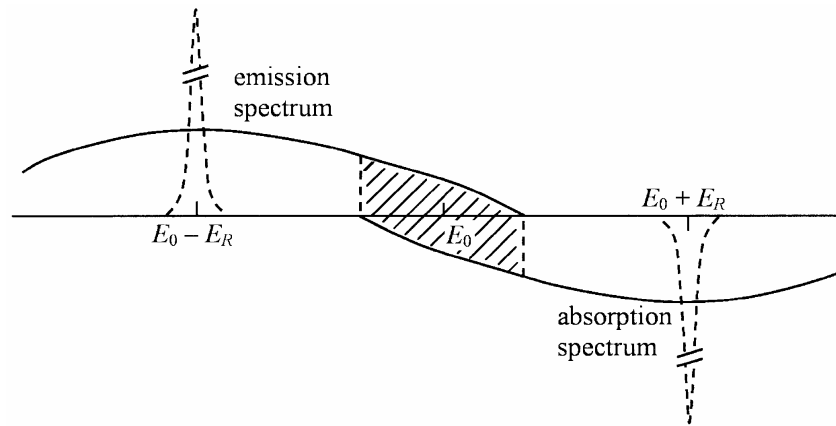
Figure 2.9: *Emission and absorption spectra of a photon considering the recoil energy of the nucleus [17]. For a non-moving nucleus the energy of the emitted or absorbed photon has a sharp peak at the energy E_0 - E_R or E_0 + E_R, respectively, whose broadening is just determined by the natural lifetime of the nucleus. The wide solid line indicates the case of a moving nucleus leading to a large Doppler broadening.*

for the photon's momentum to be absorbed by the whole crystal whose mass is so large that the emission or absorption of the photon proceeds almost recoilless.

Not all isotopes are able to undergo recoilless absorption or emission. Those which are suitable to the Mößbauer effect are called "Mößbauer active isotopes".

An important quantity considering the Mößbauer effect is the Lamb-Mößbauer-factor f_{LM} which indicates the ratio of recoil-free to total nuclear resonant absorption processes. It can be written by the formula [17]

$$f_{LM} \; = \; e^{-k^2 <x^2>} \tag{2.24}$$

with the mean square displacement $<x^2>$ of a nucleus into the direction of the emitted photon with wavevector $\vec{k}$. For a lattice with all atoms fixed to their equilibrium state, the Lamb-Mößbauer factor would be one. However, lattice vibrations reduce the value of f_{LM} and for increasing temperature more phonons lead to a decreasing Lamb-Mößbauer factor. The probability of phonon absorption or creation is given by 1-f_{LM} which is a significant value concerning the nuclear inelastic scattering experiments (Chapter 5).

2.6 Nuclear Inelastic Scattering

In this paragraph nuclear processes as the basis for the nuclear inelastic scattering (NIS) experiments (Chapter 4) are explained [18]. Synchrotron radiation is prerequisite for this method

because of the ability to tune the energy of the x-rays which is typically in the range of 20 to 40 keV for our NIS experiments. NIS is based on the Mößbauer effect, thus Mößbauer active isotopes are required. The most studied isotope is ^{57}Fe with a resonance energy of 14.41 keV. In the last years the measurements were enhanced to isotopes of higher resonance energies by using a sapphire backscattering monochromator. Those that are important for this thesis are listed in table 2.1.

	^{119}Sn	^{121}Sb	^{125}Te
Resonance energy [keV]	23.871	37.133	35.492
Recoil energy [meV]	2.58	6.12	5.41
Natural abundance [%]	8.59	57.36	7.14

Table 2.1: *List of the relevant isotopes for NIS measurements on SST.*

If an incident x-ray beam irradiates a material comprising a Mößbauer active isotope, nuclei are excited to a higher state. As every nucleus type has a different excitation energy, NIS is an isotope specific method. The decay of the nucleus bound in a solid can proceed either elastically or inelastically and in each case coherently or incoherently. However, for our measurements we concentrate on the following processes:

1. The nuclei may return to the ground state and emit a photon of the same energy as the incident one (elastic scattering). All emitted waves from several nuclei that are scattered into the forward direction are in phase, so the scattering process is coherent.

2. The nucleus may decay with the creation (or annihilation) of a phonon. The emitted photon has an energy lowered (or raised) by the vibrational energy with respect to the incident photon energy. These photons form spherical waves which occur spatially incoherent. However, normally these photons are not measured in NIS experiments because of the domination of internal conversion. In fact we detect electronic fluorescence products.

Figure 2.10 shows schematically the elastic scattering, as well as the 1-phonon and 2-phonon contribution [14]. Elastic scattering occurs for an energy of the incident photon which matches the excitation energy of the nucleus E_0. In the case of a slightly different incoming energy, a phonon can be created or annihilated, respectively, if the energy difference matches the phonon energy E_{ph}. No matter if the process occurs elastically or inelastically the finally emitted photon is delayed with a characteristic delay time corresponding to the life time of the excitation of the nuclei with respect to the absorption of the pulsed incident beam.

The decay of an excited nucleus appears either via fluorescence or via internal conversion. In the latter case, the excitation energy is transferred to an electron of the atomic shell which leaves the atom and creates a vacancy. The corresponding hole is filled up with an electron of a
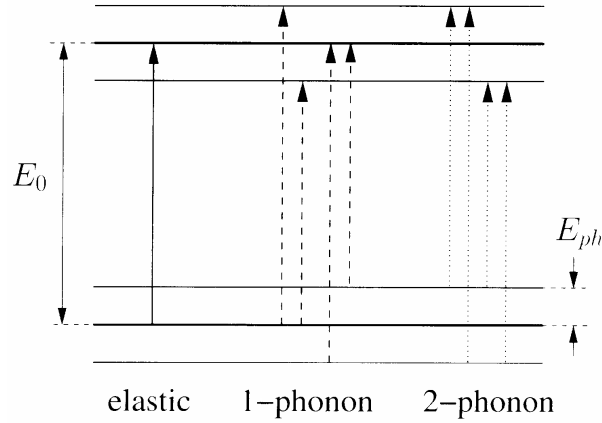
Figure 2.10: *Elastic (left) and inelastic scattering processes, the latter accompanied by the creation or annihilation of one (middle) or two phonons (right) [14].*

higher shell either followed by x-ray fluorescence or by the Auger effect. For most Mößbauer isotopes internal conversion is the dominant process.

The energy spectrum of the nuclear absorption can be separated into an elastic and an inelastic part, the latter consists of a single phonon- and a multiphonon part. The energy E is always measured with respect to the resonant energy E_0 so that positive and negative values of the energy show phonon creation or annihilation processes, respectively. The probability function for the nuclear absorption $W(E)$ can be split into terms of a multiphonon expansion [18]:

$$W(E) = f_{LM} \left(\delta(E) + \sum_{n=1}^{\infty} S_n(E) \right) \tag{2.25}$$

The quantity f_{LM} represents the Lamb-Mossbauer-factor which is also a measure for the probability of elastically scattered photons. The delta function denotes the elastic part of absorption and emission, also called the 0-phonon-term. The element S_n stands for the inelastic absorption or emission of n phonons. The 1-phonon-term is given by

$$S_1(E) = \frac{E_R \cdot g(|E|)}{E \cdot (1 - \exp(-\beta E))} \tag{2.26}$$

which means that the density of phonon states (DPS), $g(|E|)$, can be directly calculated from the 1-phonon contribution. Higher phonon terms (multiphonons) are given by the recursive equation

$$S_n(E) = \frac{1}{n} \int S_1(E') \cdot S_{n-1}(E - E') dE'. \tag{2.27}$$

In the latter equations $\beta = \frac{1}{k_B T}$ with k_B as the Boltzmann constant, the temperature T and $E_R = \frac{\hbar^2 k^2}{2M}$ the recoil energy of the free nucleus. From the 1-phonon-term of the energy spectrum, one can calculate the DPS without any further assumption.

The Lamb-Mößbauer factor is directly given by the inelastic part I(E) of the measured spectrum:

$$f_{LM} = 1 - \frac{1}{I_0} \int I(E) dE \tag{2.28}$$

with scaling factor I_0.

In order to extract further thermodynamic parameters the nth moments of the energy function

$$< E^n > = \int_{-\infty}^{\infty} W(E) E^n dE \tag{2.29}$$

are introduced. According to Lipkin [18] the 0th moment is related to the normalization of the probability function $W(E)$ and is therefore equal to unity. The 1st moment is equal to the recoil energy: $< E^1 > = E_R$. The higher order moments can be used to calculate thermodynamic parameters [18]:

- Mean kinetic energy:
$$T = \frac{1}{4E_R}(< E^2 > - E_R^2) \tag{2.30}$$

- Mean force constant:
$$F = \frac{M}{\hbar^2 E_R}(< E^3 > - 3E_R < E^2 > + 2E_R^3) \tag{2.31}$$

These parameters can also be extracted from the DPS itself which gives the possibility to check the reliability of the data treatment [19]:

- Lamb-Mößbauer factor:
$$f_{LM} = exp\left(-E_R \int_0^{\infty} \frac{g(E)}{E} \frac{1 + e^{-\beta E}}{1 - e^{-\beta E}} dE\right) \tag{2.32}$$

- Mean kinetic energy:
$$T = \frac{1}{4} \int_0^{\infty} g(E) E \frac{e^{\beta E} + 1}{e^{\beta E} - 1} dE \tag{2.33}$$

- Mean force constant:

$$F = \frac{M}{\hbar^2} \int_0^\infty g(E)E^2 dE \qquad (2.34)$$

The Lamb-Mößbauer factor is connected to the relative contribution of multiphonon excitations [14]:

$$\int S_n(E)dE = \frac{(-ln f_{\text{LM}})^n}{n!} \qquad (2.35)$$

If f_{LM} is close to unity, only few multiphonon terms contribute. A small value may occur for large transition energies or for weakly bound nuclei, i.e. also at high temperature, thus leading to a difficult separation between all phonon terms.

Additionally the heat capacity under constant volume can be extracted from the DPS [18]:

$$C_V = \left(\frac{dU}{dT} \right)_V = 3k_B \int_0^\infty g(E) \frac{(\beta E)^2 e^{\beta E}}{(e^{\beta E} - 1)^2} dE \qquad (2.36)$$

In the high temperature approximation the Debye temperature is given by:

$$\theta_D = \sqrt{\frac{3}{k_B^2 \int_0^\infty g(E) \, E^{-2} \, dE}} \qquad (2.37)$$

The Debye temperature can be used to calculate the speed of sound by the term [20]:

$$v = \frac{k_B \theta_D}{\hbar (6\pi^2 N)^{\frac{1}{3}}} \qquad (2.38)$$

2.7 Resonant Ultrasound Spectroscopy

A simple technique to measure the speed of sound of a thin film is based on the propagation time of a wave inside a medium. An acoustic wave pulse of high frequency is introduced at a polished face of the sample by the use of a transducer and is reflected at the parallel face [21]. This is known as the pulse echo method. In this case the speed of sound v is determined as the fraction of the length l of the sample and the propagation time t:

$$v = \frac{2l}{t} \qquad (2.39)$$

Unfortunately, the quality of the results of this technique relies very strongly on the accuracy of the propagation-time measurement. Physical effects such as attenuation, diffraction, dispersion and propagation anomalies inside the sample influence the shape and the amplitude of the wave during propagation [22]. Considering a 1 cm long sample, a pulse moving with typically 5000 m/s needs 4μs to travel through the sample and back, so a timing accuracy in the ns range is required. Smaller samples require even shorter pulses leading to an even more difficult time measurement.

Another technique which is based on the resonant character of solids is resonant ultrasound spectroscopy (RUS) [22]. The sample is excited to undergo mechanical oscillations of different frequencies. The measured spectrum is dependent on the geometry of the sample and shows sharp peaks at the resonance frequencies of the sample. The positions of the resonance energies can be used to determine the elastic constants of the material. For this purpose we calculate the equilibrium state of a system by minimizing the Langrangian:

$$L \; = \; T - V \tag{2.40}$$

with the kinetic energy T and the potential energy V. For an arbitrarily shaped elastic solid the kinetic and potential energy are given by:

$$T \; = \; \frac{1}{2} \sum_i \rho \omega^2 u_i^2 \tag{2.41}$$

$$V \; = \; \frac{1}{2} \sum_{i,j,k,l} c_{ijkl} \frac{\partial u_i}{\partial x_j} \frac{\partial u_k}{\partial x_l} \tag{2.42}$$

where x_i represents the x, y or z-coordinate and u_i are the directions of the displacement vector. ρ is the density, ω the angular frequency and c_{ijkl} the components of the elastic stiffness tensor. Generally the elastic stiffness tensor $\vec{\vec{C}}$ is of fourth order but due to symmetry reasons it can be represented by a 6x6 matrix [21]. Physically it depicts the resistance on deformation of a material by connecting the elastic stress σ and strain ϵ (Hooke's law):

$$\vec{\sigma} \; = \; \vec{\vec{C}}\vec{\epsilon} \tag{2.43}$$

Due to symmetries in the material for a cubic or an isotropic medium, the matrix is reduced to only three and two independent components, respectively. For the isotropic medium, these are c_{11} and c_{44}, whereas c_{44} is equal to the shear modulus G and describes the response of a material to a shearing strain.

In order to minimize the Langrangian function (Equation 2.40), the displacement vector is expanded into a complete set of functions ψ_λ (Rayleigh-Ritz method) [22]:

$$u_i \;=\; \sum_\lambda a_{i\lambda}\psi_\lambda \tag{2.44}$$

By choosing a Visscher basis set using simple powers of the cartesian coordinate system [21], one yields the eigenvalue equation

$$\omega^2 \vec{\vec{E}}\vec{a} \;=\; \vec{\vec{\Gamma}}\vec{a} \tag{2.45}$$

where the components of $\vec{a}$ are the expansion coefficients a_i and the elements of the matrices $\vec{\vec{E}}$ and $\vec{\vec{\Gamma}}$ are given by [22]:

$$E_{\lambda i \lambda' i'} \;=\; \delta_{ii'} \int_V \psi_\lambda \rho \psi'_\lambda dV \tag{2.46}$$

$$\Gamma_{\lambda i \lambda' i'} \;=\; \sum_{j,j'} c_{iji'j'} \int_V \frac{\partial \psi_\lambda}{\partial x_j}\frac{\partial \psi'_\lambda}{\partial x_j}\,dV \tag{2.47}$$

Equation 2.45 can be solved numerically by standard eigenvalue solution techniques [21]. Knowing the density ρ and the resonant frequencies ω of a material, the elastic constants are obtained in such way.

According to the Kelvin-Voigt model [21], the speed of sound in an isotropic solid is divided into a longitudinal v_l and a transversal part of the velocity v_t. These components are given by the elastic constants:

$$v_l \;=\; \sqrt{\frac{c_{11}}{\rho}} \tag{2.48}$$

$$v_t \;=\; \sqrt{\frac{c_{44}}{\rho}} \tag{2.49}$$

Chapter 3

Sample Preparation

Two different methods were chosen in order to prepare the $SnSb_2Te_4$ (SST) samples. Both techniques were used in the "I. Physikalisches Institut" at the RWTH Aachen. Using the first technique which is based on vapour deposition, we were not able to prepare a sample with a clearly defined phase. Thus a second method was considered which is based on magnetron sputtering. The advantage of this method was the possibility to cool the substrate during the preparation process. In this chapter both techniques are presented in detail and their advantages and disadvantages are discussed.

3.1 Vapour Deposition

3.1.1 The KOMA-facility

The SST samples were prepared at the KOMA-facility (Kombinatorische Materialsynthese - combined material synthesis) (Figure 3.1). For a detailed description of this instrument see [9]. The principle of this technique is based on vapour deposition of the single elements onto a substrate.

The machine consists of two different chambers separated by gate valves, the preparation chamber and the analysis chamber. A sluice connects a load lock with the preparation chamber so that new substrates can be loaded without breaking the vacuum. Substrates and samples can be transported inside the chamber using a wobble stick. The 2x2 cm substrate is located in the centre of the chamber on a stainless steel sample holder with a distance of 10 cm to each of the nine crucibles at the opposite side. The main problem in the use of this technique was that the temperature of the substrate cannot be measured or controlled during the preparation with subsequent problems in obtaining amorphous samples (see Chapter 4).
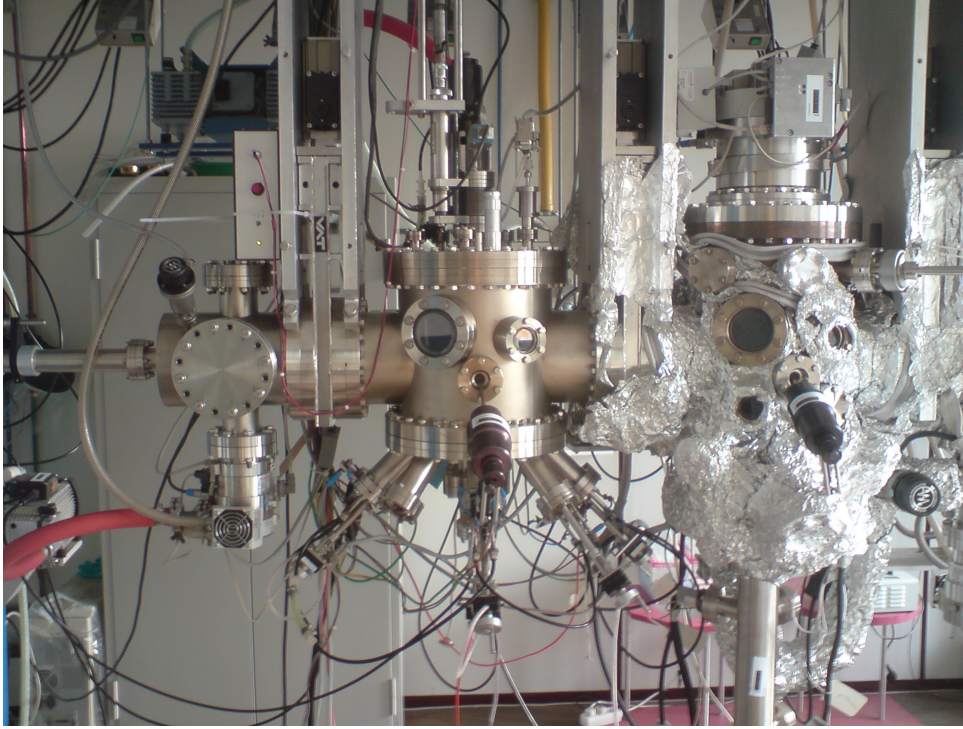
Figure 3.1: *A close up of the KOMA-facility. The preparation chamber with the crucibles attached at the bottom is in the center.*

The preparation chamber is evacuated by a turbomolecular pump to a base pressure of about 10^{-8} mbar. The deposition rate is measured during the preparation utilizing a self constructed, water-cooled quartz balance. For the actual preparation process, the quartz balance has to be moved away from to the substrate electronically, thus the deposition rate cannot be measured synchronously. The quartz balance oscillates with its resonant frequency which is dependent on the total mass m. The film thickness can be calculated by the formula

$$d_f \propto \frac{1}{f_c \rho_f Z} \arctan(Z \tan(\pi \frac{f_q - f_c}{f_q})) \tag{3.1}$$

with the resonance frequency of the quartz crystal f_q and of the crystal and the deposited film f_c. In order to measure the deposition rate of a specific element the density ρ_f and the material constant Z (so called Z-factor) have to be known. The Z-factors for Sn, Sb and Te are 0.724, 0.768 and 0.9, respectively.

Up to nine evaporation sources can be installed at the lower side of the machine and up to four can be utilized simultaneously. Each of them is connected to the chamber utilizing a flange as well as a viton ring providing the possibility of ultra high vacuum conditions. The sources can be separated from the substrate and the quartz balance by a master shutter which is controlled by a computer software. Eight evaporation sources are tilted by an angle of $45°$ with respect to

the substrate and one is located directly under the substrate. The substrate can be rotated which additionally to the inclination of the sources increases the homogeneity of the deposited film.

For the evaporation sources, Knudsen cells were chosen as shown in Figure 3.2 as a close-up view. Its name is given by Martin Knudsen, a Danish physicist from the late 19th and early 20th century. The main part of the Knudsen cell consists of an Al_2O_3 crucible containing the material for evaporation. It is wrapped by a molybdenum foil which thermally isolates the crucible from the surrounding in order to ensure stable evaporation rates. An individual shutter isolates the crucible and can be controlled manually or automatically by a stepper motor. The temperature control of the crucible is performed by using an adjustable power supply providing 1 to 10 Volts DC. The constant voltage is applied to a filament of tantalum wire. The temperature is measured by a thermocouple close to the crucible. Both the stepper motor for crucible shutters and the temperature control are operated by a special computer software. The maximum possible temperature in a crucible is limited by the power supply and the filament to about 1200°C. Furthermore two additional feedthroughs are implemented in the Knudsen cell in order to provide the water cooling.
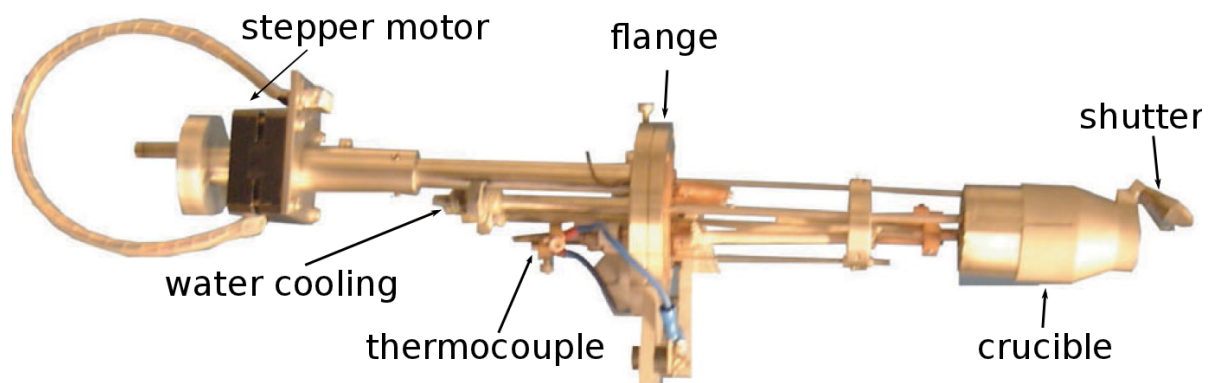
Figure 3.2: *The Knudsen cell which was used as evaporation source [9]. The material is located inside the crucible which is opened and closed electronically by a shutter.*

The crucible is depicted in Figure 3.3. To obtain pure films it is crucial that the crucible and evaporating material are chemically inert for all relevant temperatures. For this purpose the crucibles are made of the ceramics Al_2O_3. The aperture has a diameter of 5 mm and the total length of the crucible is 33 mm.

3.1.2 Deposition Process

For the preparation of the chosen compound $SnSb_2Te_4$ we started from the three single elements Sn, Sb and Te. Sn was enriched to 92% in ^{119}Sn, Te was enriched to 75% in ^{125} Te and Sb has a sufficiently large natural enrichment of 57% ^{121}Sb.
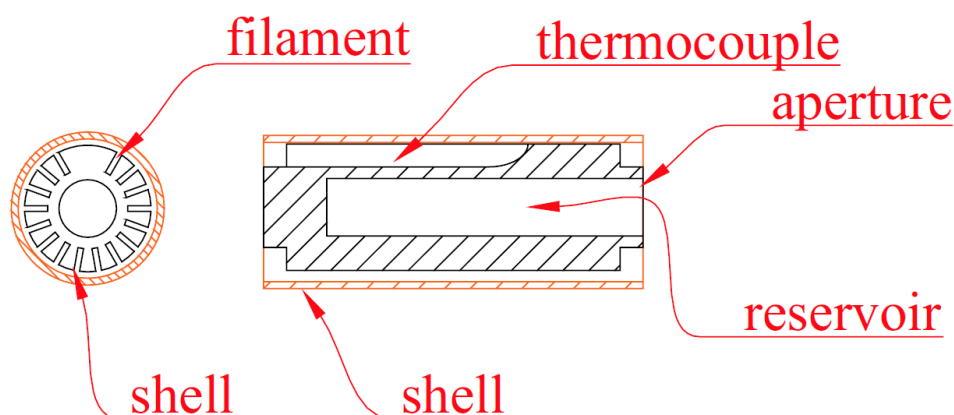
Figure 3.3: *The crucible seen from the top (left) and from the front side (right) [9]. It is wrapped by a tantalum filament in order to heat the crucible. The thermocouple is very close to the crucible.*

In order to match the appropriate deposition rate for each element, first the required evaporation temperatures had to be found. The temperatures for Sb and Te were in the range of 250°C and 320°C, respectively. However, the quartz balance did not show any deposition rate for Sn even at 1200°C. The material partly disappeared from the Sn-crucible and the balance also exhibited a slight visual film on top. It is important to note that the melting temperature of Sn is at 232°C and the vapour pressure at 1000°C should be large enough to evaporate (10^{-4} to 10^{-5} Torr). Probably there was some SnO formed at the surface, however, this phenomenon has not been resolved yet.

This problem was solved by preparing an alloy of enriched ^{119}Sn with a natural abundance in Te. Using induction heat both isotopes were melted and a ^{119}SnTe compound was formed which functioned as substitute material for Sn. Finally SnTe evaporated successfully in the KOMA facility at a temperature of about 450°C. Because $SnSb_2Te_4$ is now synthesized with $1 \cdot ^{119}SnTe + 2 \cdot ^{121}Sb + 3 \cdot ^{125}Te$, the evaporation rates have to be adjusted in order to match the correct stoichiometry.

Because the evaporation rate is given in Ås^{-1}, it does not necessarily correspond to the stoichiometric indices of the single element inside the ternary compound. The number of atoms in a special layer thickness depends on the density of the material which is, of course, different for Sn, Sb and Te. In order to calculate the evaporation rate, one has to weigh the coordination number of every constituent part with its density. The final parameter for SnTe, Sb and Te had ratios of 1.0, 2.2 and 3.5, respectively.

The deposited sample finally had a thickness of about 2μm on a 2x2 cm aluminium substrate. However, the temperature during the preparation was not controlled so the phase of our deposited material was unknown. In Chapter 4.1 both the phase and the stoichiometry of our samples will be characterized via x-ray diffraction.

3.2 Magnetron Sputtering

Magnetron sputtering was the second method that we applied to prepare $SnSb_2Te_4$ (SST) samples with appropriate phase and stoichiometry. X-ray diffraction in Chapter 4.1 will reveal that the KOMA-samples described in the previous chapter were not deposited in the required amorphous phase due to the missing temperature control during the preparation. So it was essential to find a new technique which offers cooling equipment for our substrates.

3.2.1 Instrumentation

Sputtering is a common deposition process to prepare homogeneous thin films in various ranges of thicknesses. It is based on the bombardment of a target with ions and the subsequent condensation of the free target atoms on a substrate. Our sputter-runs were performed at the magnetron sputtering facility at the RWTH Aachen. The utilized machine is presented in Figure 3.4.

Figure 3.4: *A close-up of the Sputter-facility.*

The principle of the technique is shown in Figure 3.5. On the upper side of the sputtering chamber there are up to four substrates facing upside down. On the bottom side there are up to four different targets each fixed on a permanent magnet. Additionally between target

and substrate different kinds of masks can be placed which ensure a more homogeneous film growth. The sputtering chamber is first evacuated to a base pressure of about 10^{-6} mbar and purged with an inert process gas (Ar). In order to prevent water condensation during the sample exchange the walls and inner components of the chamber are heated. Between the inner walls of the chamber and the target a DC high voltage is applied with the target working as cathode. Free electrons are accelerated by the electric field and ionise the Ar-atoms, so that a plasma of Ar-ions and free electrons is formed. These newly formed free electrons are called secondary electrons and again ionise other Ar-atom so that the ionisation process is amplified. The positive ions are accelerated onto the negatively charged target and produce collision cascades. Neutral target-atoms are ejected and distributed randomly inside the chamber. They condensate all over the chamber as well as on the substrate where a thin layer is formed whose stoichiometry matches the one from the target material.

The magnet below the target creates a magnetic field which forces charged carriers on spirals due to the Lorentz force. However, the much heavier Ar-ions are hardly affected by the magnetic field while electrons are kept close to the target. This condition raises the number of ionised atoms and hence the sputter-rate. Due to the incorporation of a magnetic field this special technique is called magnetron sputtering.
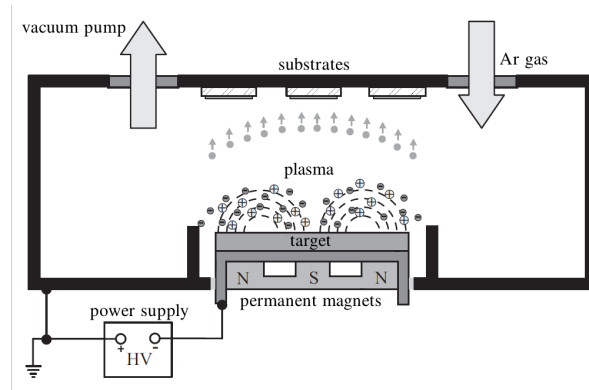
Figure 3.5: *A schematic illustration of the magnetron sputtering setup [23]. The Ar gas is ionised by free electrons which are accelerated by the electric field. The Ar-ions produce collision cascades at the target. Neutral target atoms are ejected and distribute inside the chamber.*

The sputtering instrument gives the opportunity to perform static as well as dynamic sputtering. Whereas in the case of static sputtering only one substrate can be processed, in the dynamic mode up to four substrates are rotating above the plasma simultaneously and are deposited at the same time.

An additional important feature of this magnetron sputterer is an optional cooling system. This special home-made device is connected via pipes to a liquid nitrogen source, thus the cooling system can only be applied in the static mode. Figure 3.6 shows the build up of the cooling

unit. It consists of a sample holder (1) which contains the substrate (2) and a copper block (3) fixed to the sample holder. This arrangement guarantees a close contact to the substrate. The copper block is actually a small reservoir of about 20x20x20 mm connected to a liquid nitrogen source. Thus a constant nitrogen flow ensures the reduction of thermal energy on the sample.
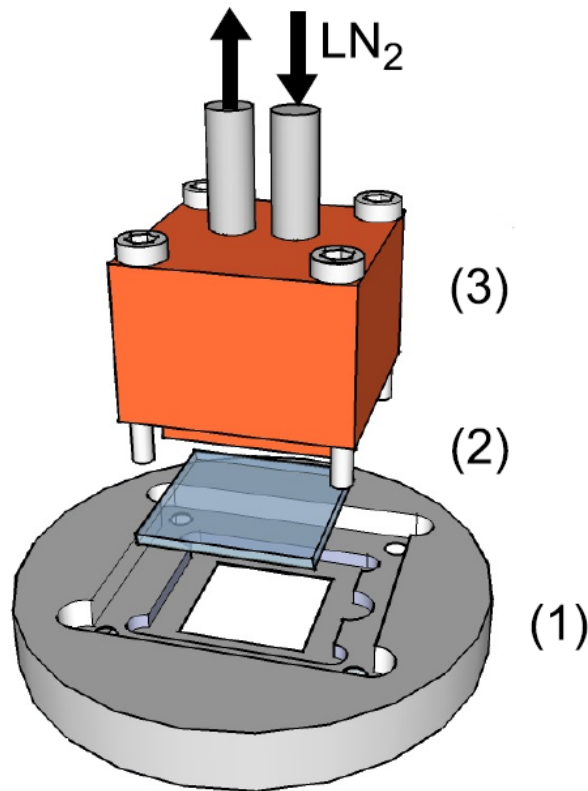
Figure 3.6: *A sketch of the specially developed cooling system [23]. It consists of the sample holder (1), the substrate (2) and a copper block (3). The copper block is cooled by liquid nitrogen.*

To measure the temperature during the preparation a type K thermocouple is fixed on the copper block and is connected to a multimeter outside the chamber. In Ref. [23] it was reported that the temperature at a quartz glass (SiO_2) substrate is unfortunately almost 100 K higher than at the copper block, at least for low temperatures. However, the thermal conductivities of silicon (150 W/mK), aluminium (235 W/mK) and aluminium nitride (180 W/mK) which were used in this case are much larger than of quartz glass (around 1 W/mK). Nevertheless one has to consider this circumstance during the preparation.

3.2.2 Sputtering Process

Several batches of samples have been sputtered on different substrates. For nuclear inelastic scattering (NIS) (Chapter 5) the samples were sputtered on an aluminium foil attached to a

silicon plate. For resistivity measurements we chose AlN because electrically isolating substrates were required (Chapter 4.2) and special GaAs substrates for the resonant ultrasound spectroscopy (RUS) measurement (Chapter 4.3). A large thermal conductivity is important for all substrates in order to ensure a good thermal coupling to the cooling system. Efficient cooling is required in order to obtain a pure amorphous phase. The sputter-power was adjusted to 20 W, the base pressure was in the range of $3 \cdot 10^{-6}$ mbar and Ar with a purity of 99,999 % was used as sputter gas. Before every run a dwell sputtering procedure of 1800 s was performed in order to get rid of oxygen layers formed on the surface of the target material.

The sputtering temperature was measured at the copper block which is reported [23] to be different from the actual substrate temperature. Therefore the system was cooled to temperatures between -100°C and -70°C to ensure that the sample temperature during the sputtering process was far below the crystallization point (about 130°C). At the end of every sputter process the chamber was filled with nitrogen used as heat exchange in order to rapidly cool the system back to room temperature. After about 20 minutes the sample reached a temperature of 15°C.

For most of the samples a final thickness of about 250 nm was intended to prevent a peeling off of the samples from the substrates. Especially during defrosting restrains of the film can occur resulting in a detaching from the substrate. The static sputtering-rate for SST was 1.038 nm/s [23], resulting in a sputter-time of 241 s in order to achieve the chosen thickness.

For the RUS sample, however, specific conditions had to be fulfilled. The substrate needs to have a volume of about 1 mm^3 and all opposite planes must be parallel (Chapter 2.5). For this purpose we chose GaAs with a thickness of 0.3 mm. Because the sample thickness should be at least 1/1000 of the substrate thickness we decided to sputter for 520 s which is equivalent to a final film thickness of about 540 nm. The GaAs substrates were glued on a 2x2 cm copper plate in order to fit into the sample holder of the sputterer. For further details about the RUS samples, see Chapter 4.3.

3.3 Annealing the Samples

The primary aim concerning $SnSb_2Te_4$ (SST) was to obtain samples on appropriate substrates for nuclear inelastic scattering (NIS), resistivity and resonant ultrasound spectroscopy (RUS) measurements. Table 3.1 shows an overview of the measured samples with the substrate and the thickness of the film.

The as-deposited samples were characterized via x-ray diffraction (Chapter 4.1) and revealed a clear amorphous phase for the sputtered samples, however, a mixture of both crystalline phases

Measurement	Substrate	Thickness
NIS	Al foil	2000 and 250 nm
Resistivity	AlN	250 nm
RUS	GaAs	540 nm

Table 3.1: *Measurement type, substrate and thickness of the measured samples.*

was observed for the as-deposited KOMA samples. To obtain the required crystalline phases, the prepared samples were switched by annealing to the phase specific temperature.

The KOMA sample was used as the basis for a hexagonal phase. Knowing that the hexagonal phase is the stable phase of SST at high annealing temperatures, the sample finally was annealed at 150°C for 12 hours. The base pressure in the furnace was 10^{-3} mbar to prevent oxidation during the annealing.

In order to switch to the cubic phase, one amorphous sample prepared via magnetron sputtering was chosen. In order to find the correct switching temperature the sample was annealed to a series of temperatures for several hours with a subsequent characterization using x-ray diffraction. It was important not to heat up too quickly because just a small overshoot could switch the sample irreversibly at least partially into the hexagonal phase. An estimation for the appropriate temperature was given by $GeSb_2Te_4$ data whose temperature range for the stability of the cubic phase lies at around 120°C to 200°C. The starting temperature for our experiment was 110°C with steps of around 5°C. Finally, the cubic phase was obtained after annealing to 133°C for 48 hours.

Chapter 4

Characterization Techniques

In this chapter different measurements are presented which were performed in order to get information about macroscopic parameters on $SnSb_2Te_4$ (SST). Other properties such as heat capacity or reflectivity were not determined within this work but could be considered for future projects in order to establish a full characterization of this material. However, the important parameters that yield knowledge of the appearance of different phases inside the material as well as their transition temperatures, were investigated.

Starting with x-ray diffraction the purity of the phases and crystallographic symmetry of SST was determined. Furthermore a profile matching was performed in order to extract structural parameters such as lattice constants. Temperature dependent resistance measurements in a self-build high temperature furnace were performed between room temperature and 300°C in order to determine the resistivity of SST in all three phases and, more importantly, the transition temperatures between the phases. Finally resonant ultrasound spectroscopy (RUS) was performed because it is a unique method to determine elastic constants and the speed of sound of thin layers.

The properties of SST obtained in this chapter are compared with those of $GeSb_2Te_4$ (GST).

4.1 X-ray Diffraction

4.1.1 Instrumental Features

X-ray diffraction experiments were performed using the Huber G670 Guinier Camera. A schematic set up of the instrument is shown in Figure 4.1. The x-rays produced by an x-ray tube are monochromatized using a Ge (111) reflection in order to select the Cu $K_\alpha 1$ radiation (wavelength 1.54 Å). The sample is fixed on a sample holder which oscillates horizontally during the measurement in order to illuminate a representative area of the sample and to reduce

texture. The x-rays are diffracted by lattice plains and interfere constructively if Bragg's law is fulfilled. The linear image plate detector records the diffracted radiation in an angle between $20°$ and $100°$ with respect to the incident beam. All measurements were performed at ambient conditions for 60 minutes.
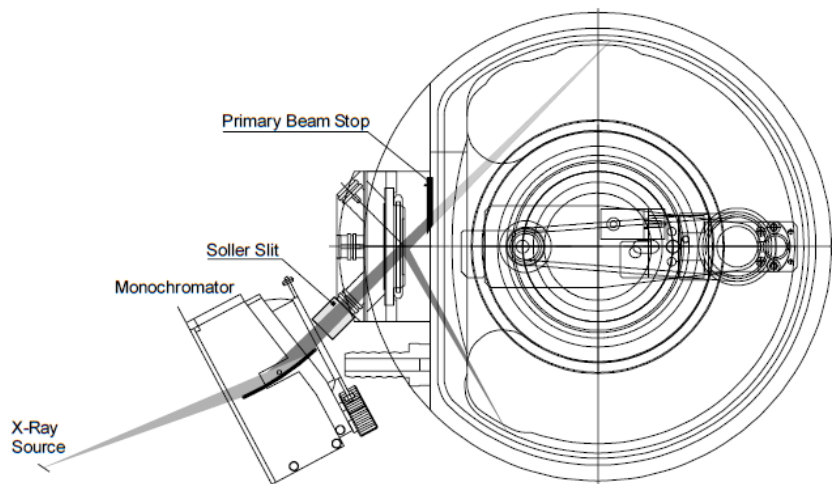
Figure 4.1: *Top view of the Guinier Camera used for x-ray diffraction [24]. After the x-rays are monochromatized, one part of the beam is diffracted by the sample and the other part is transmitted.*

4.1.2 Interpretation of the Diffractograms

Both samples prepared via vapour deposition and via magnetron sputtering were characterized with x-ray diffraction. Representative results for each preparation technique are shown in Figures 4.2 and 4.3. In both cases the lowest curve indicates the aluminium substrate which is different for the two preparation techniques. All samples deposited on aluminium substrates could be measured with this method using transmission geometry. The sputtered samples on AlN and GaAs are assumed to be in the same as deposited phase.

The x-axis represents the 2θ value of the diffracted beam and on the y-axis the intensity of scattered radiation is plotted in arbitrary units. The momentum transfer is also given on the top axis represented by the scattering vector q. In Figures 4.2 and 4.3 the aluminium peaks are indicated with their Miller indices and hatched out. Some peaks in the sputtered samples could not be identified and are hatched by smaller boxes. Because all the hatched peaks also occur in the substrate, they are not indicative for the sample properties.

Especially because of the missing temperature control during the preparation, it was crucial to investigate the phase of the KOMA samples. The diffraction from the as deposited sample is depicted as the violet line in Figure 4.2. By comparison with the aluminium substrate (lower

curve) one sees five additional peaks which are a clear indication for a non-amorphous phase. The peaks could be identified as cubic peaks with the Miller indices labelled at the bottom of the diagram. Whereas the (2 2 0), (4 2 0) and (4 2 2) fit with the theoretical position, the (2 2 0), (2 2 2) and (4 0 0) peaks are shifted to lower angles. The (4 0 0) peak even is very flat and differs by almost 3° from its expected position. Furthermore the measured peaks reveal a large FWHM which indicates that the crystalline phase does not form large crystallines yet. This leads to the assumption that this phase is partially cubic and hexagonal, i.e. the sample did not crystallize to the hexagonal phase completely. Despite a crucible to sample distance of about 10 cm, a maximum (SnTe-) crucible temperature of almost 1000°C and a deposition time of about 20 minutes lead a processing temperature that was probably too high to prepare an amorphous sample.

Because of the (practically) irreversible switch, the sample prepared via vapour deposition in the KOMA facility was neither appropriate as amorphous nor as cubic sample. Therefore it was annealed to 150°C so that it completely switched to the stable hexagonal state. The x-ray diffractogram is shown as the red curve in Figure 4.2. In this case the reflections appear much sharper and they are shifted into the expected position of the hexagonal phase. This strengthens the argumentation of the mixture phase for the as deposited sample. The annealed sample shows the hexagonal structure and will be called "hexagonal" from now on.

Because the KOMA samples can just be used to obtain the hexagonal variant, magnetron sputtering was utilized with the opportunity to control the temperature during the preparation. The characterization of the so produced samples is shown as the green line in Figure 4.3. The curves of as-deposited phase and the substrate hardly differ from each other. The (aluminium) peak positions are identical, only the intensities of the first three aluminium peaks are lowered significantly which is due to absorption of the sample. This sample functions as amorphous sample.

One of the sputtered samples was switched into the NaCl structure which exists in a certain temperature range (Chapter 4.2). The x-ray diffraction result is shown as blue line in Figure 4.3. One observes six well-defined peaks labelled with the corresponding Miller indices. However, the peaks reveal a quite large FWHM which is due to crystallization within small regions.

The size of the crystallites were calculated utilizing the Scherrer-equation [25]

$$\Delta = \frac{K\lambda}{L\cos\theta_0} \tag{4.1}$$

which provides a lower bound for the average size of a scattering object L in the sub-micrometre range. The width of the peaks Δ depends on position of the peak θ_0, the incident wavelength λ and the Scherrer form factor K which is close to unity. For this purpose all six
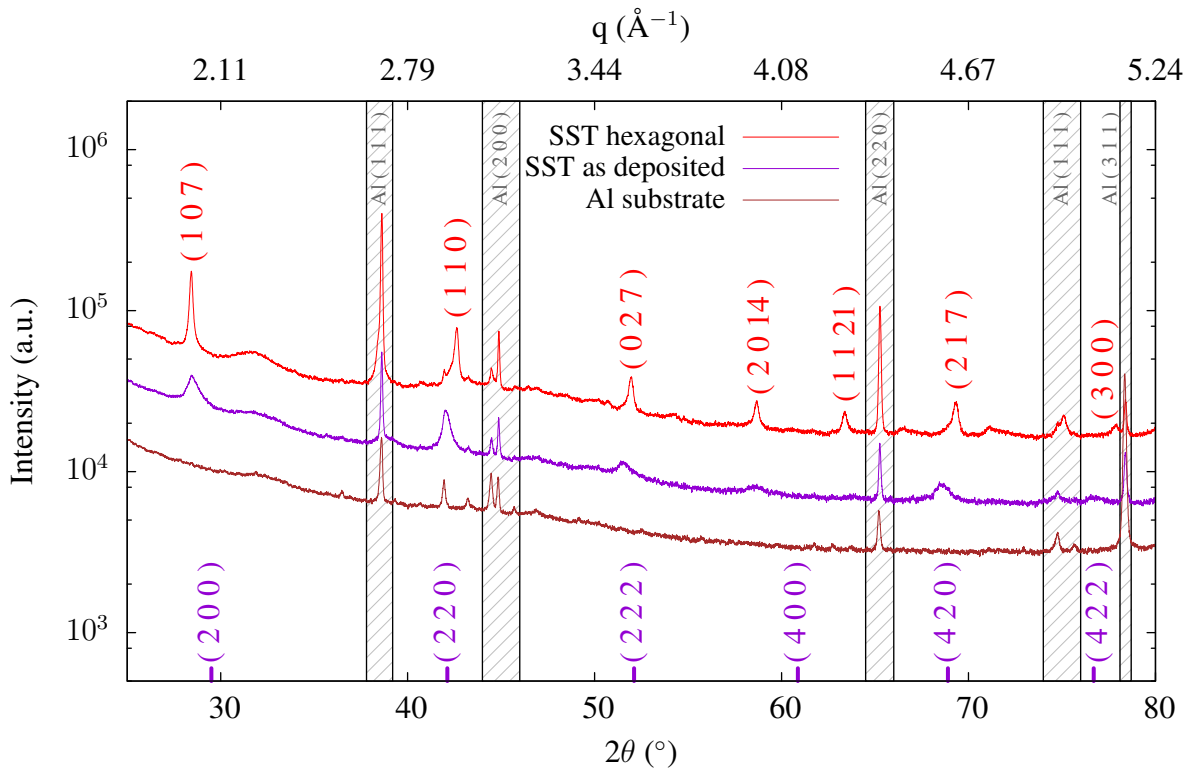
Figure 4.2: *XRD measurement of the samples prepared via vapour deposition presented in logarithmic scale. The brown, purple and red curves show the substrate, the as-deposited phase and the hexagonal phase, respectively. The as-deposited sample shows additional peaks with respect to the substrate, hence it is not in the amorphous state. The annealed sample shows a hexagonal structure with all peaks indicated with the corresponding Miller indices.*

sample peaks were fitted by a Gaussian profile to determine the position and the FWHM of every peak (Table 4.1).

	(2 0 0)	(2 2 0)	(2 2 2)	(4 0 0)	(4 2 0)	(4 2 2)
2θ [°]	29.247(1)	41.871(2)	51.862(4)	60.622(7)	68.946(4)	76.546(7)
FWHM [°]	0.464(3)	0.613(5)	0.646(15)	0.594(21)	0.493(13)	0.908(34)

Table 4.1: *2θ values and FWHM obtained by fitting the cubic peaks by a Gaussian profile.*

Applying the Scherrer equation, leads to an average crystallite size of 97 ± 9 Å. Maybe the cubic sample is still not completely switched to the NaCl structure and did not form a spatially homogeneous film. In comparison, the hexagonal sample revealed much larger crystallites (> 400 Å).

By fitting all peaks with a Gaussian profile the 2θ positions were determined to calculate the lattice constants of the cubic SST phase. The zero shift of the instrument was set to 0.32° established with a reference material. The manually calculated lattice constant was 6.162 ± 0.002 Å and will be confirmed in the next paragraph.
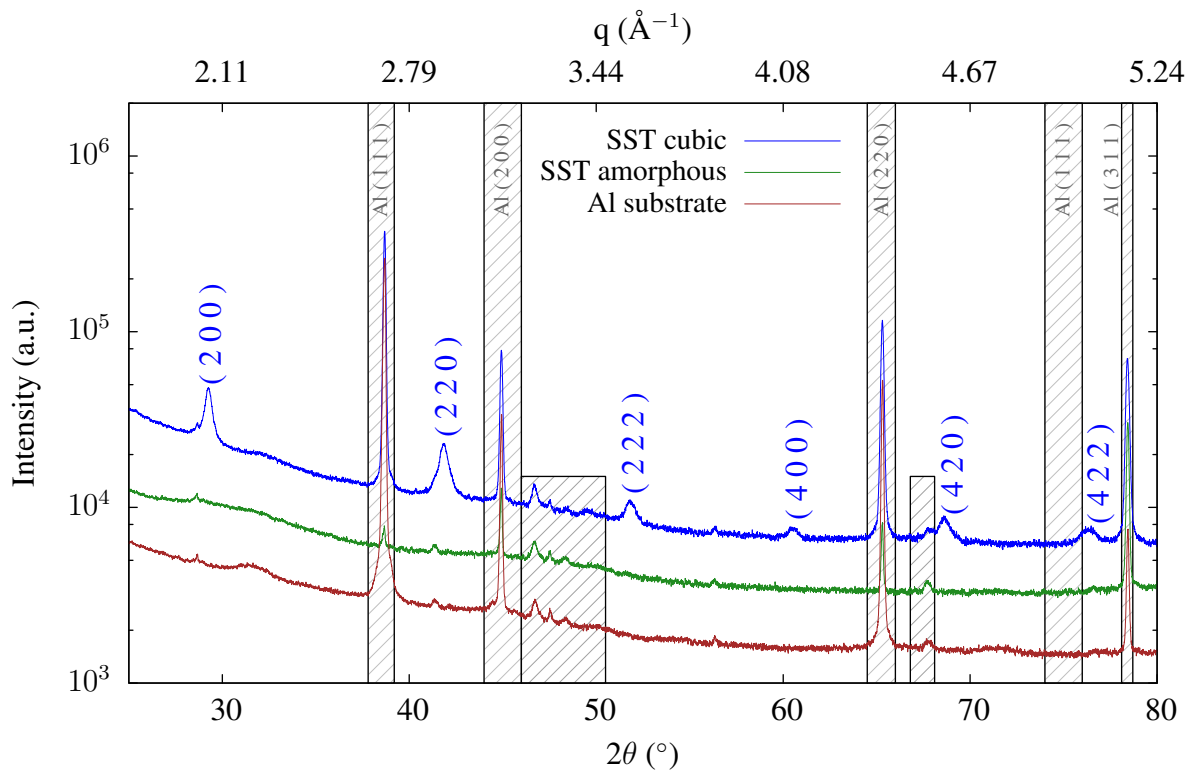
Figure 4.3: *XRD measurement of the samples prepared via magnetron sputtering presented in logarithmic scale. The green curve, indicating the as-deposited sample, is purely amorphous. The annealed sample (blue curve) exhibits cubic peaks depicted with their Miller indices, however, revealing a large FWHM.*

4.1.3 Profile Matching

A profile matching of the x-ray data described in the previous chapter was performed with the software FullProf. Both the cubic and the hexagonal data could be refined adequately and structural parameters were obtained. The refinement is demonstrated in Figures 4.4 and 4.5. The red line represents the data, the black line the fit to the data and the blue line symbolizes the residuals between measurement and fit. The aluminium peaks were excluded from the procedure.

The x-ray data of the NaCl-structured SST sample (Figure 4.4) shows a very good match with the fit which is also expressed by the residual. The χ^2 of this fit was 2.14 per degree of freedom which is a satisfying result. The obtained lattice parameter is 6.165 ± 0.003 Åwhich is very close to the manually calculated one.

The hexagonal data shows a good result, too, although the χ^2 is quite large with 4.72. The lattice constants are extracted with a good precision to a = 4.252 ± 0.001 Å, c = 42.625 ± 0.001 Å.

The results for the lattice constant and the size of the crystallites are summarized in table 4.2.
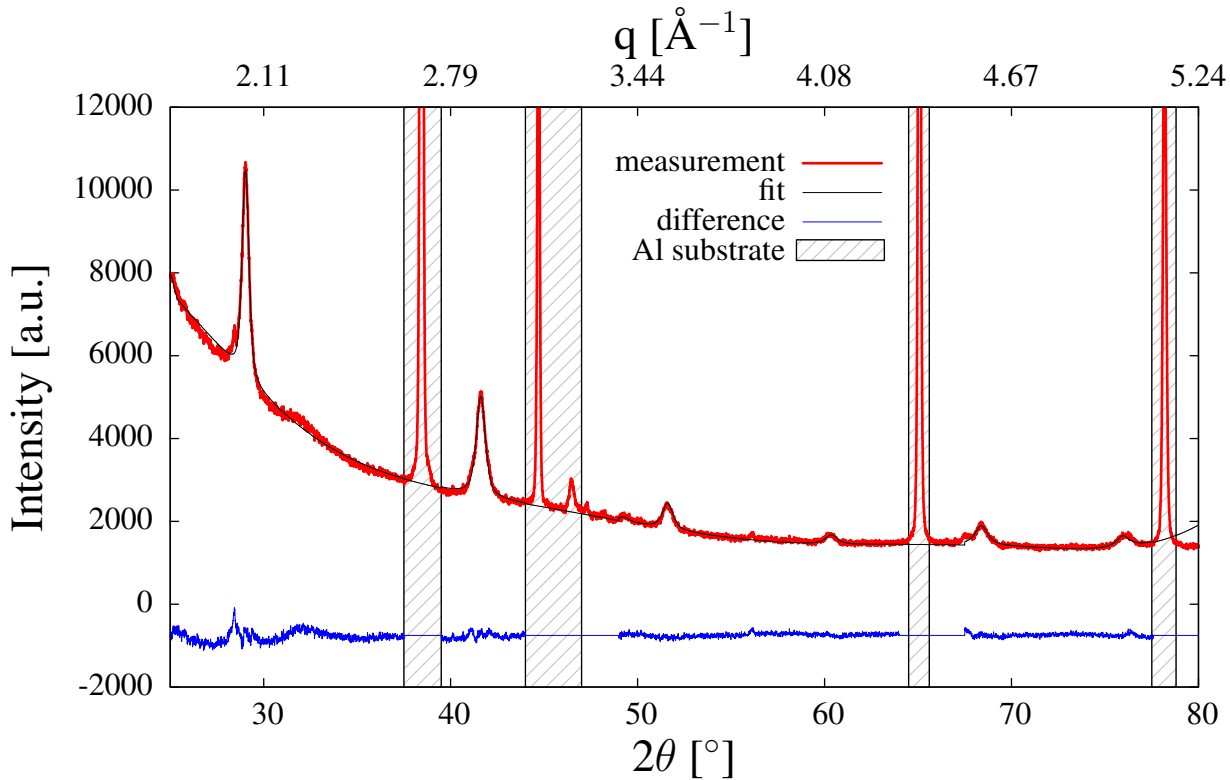
Figure 4.4: *Profile matching of the cubic sample. The blue line depicts the residual and the Al peaks are hatched out. The fit (black) is in good agreement with the data (red).*

	Cubic	**Hexagonal**
Lattice constants [Å]	6.165(3)	a = 4.252(1), c = 42.625(1)
Crystallites [Å]	97(9)	> 400

Table 4.2: *Lattice constants and crystallite sizes obtained from the XRD measurements.*

Finally, the obtained lattice constants of SST are compared with those of GST. The value for the lattice constants of GST are 6.043 Å for the cubic phase and a = 4.272 Å, c = 41,686 Å for the hexagonal state [26]. According to the lattice constants, the substitution of Ge with Sn has just a small impact on the lattice dimensions. The Sn atom has more electrons and therefore a slightly lower electro negativity (1.8) than Ge (2.0) which leads to larger distances between Sn and Te atoms in both crystalline structures. Only the smaller hexagonal lattice parameter does not change significantly which is probably due to a domination of Te and Sb atoms in this dimension.

4.2 Four Probe Resistivity Measurement

Temperature dependent resistivity measurements were performed and the precise phase transition temperatures were defined for SST. Furthermore the resistivity for all three phases of this
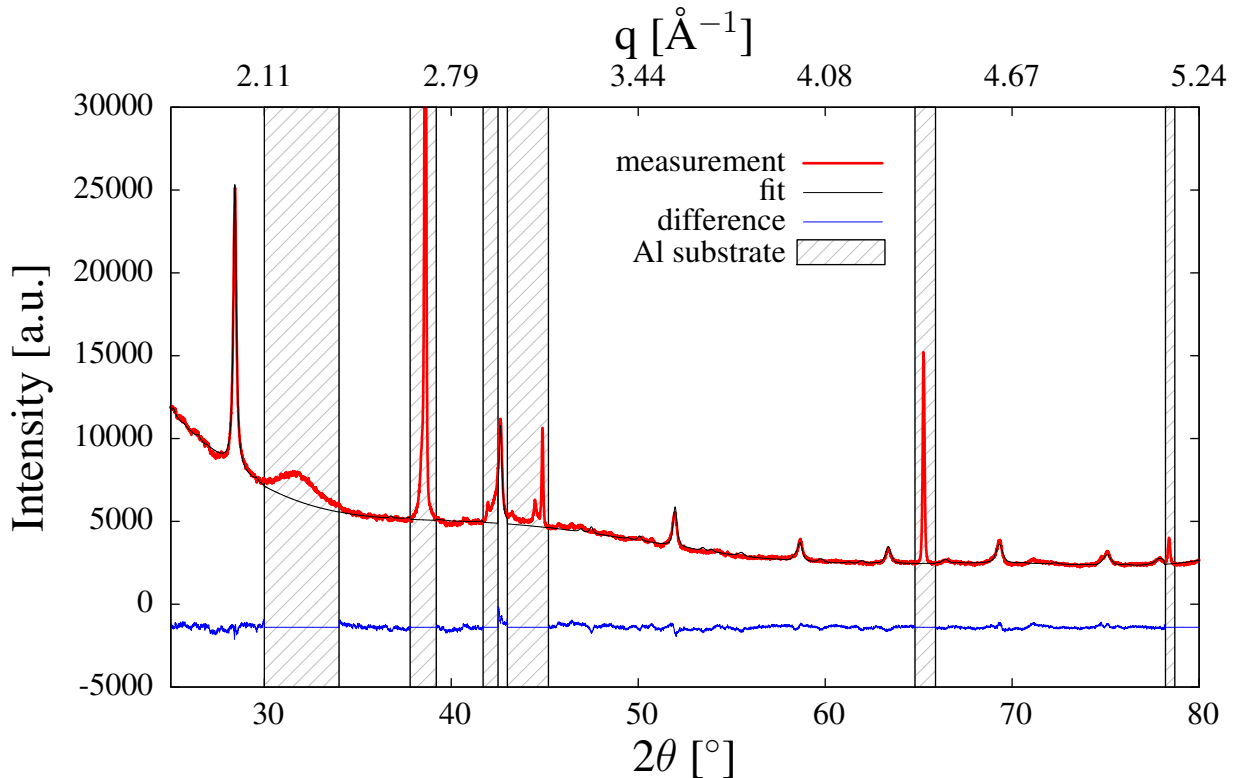
Figure 4.5: *Profile matching of the hexagonal sample. The substrate peaks are hatched out. The fit (black) is in good agreement with the data (red). The blue curve represents the difference between measurement and fit.*

material could be extracted as a macroscopic parameter and be compared to values for GST. In order to obtain precise data, a four point probe was used.

4.2.1 Construction of a High Temperature Sample Holder

In order to measure resistance of SST a high temperature furnace (T_{max} = 1200 K) was used. Inside the furnace a quartz tube provides the possibility to evacuate the chamber in order to prevent oxidation of the material during heating. At the bottom of the quartz tube there is a connection to a vacuum pump and on the top there is a hole to place a cover with e.g. feedthroughs for contacts. In order to perform the electrical resistance measurement under special conditions (high temperatures, in vacuum), a special sample holder was built which fits inside the glass tube and makes it vacuum tight. Special care was taken for all components of the sample holder to be high temperature resistant.

A sketch of the constructed sample holder is shown in Figure 4.6. The framework of the sample holder is made of Al_2O_3 parts (melting point about 2000°C). It consists of four, approximately 40 cm long, parallel bars and several ceramic plates with a diameter of about 6 cm. The plates are placed in order to stabilize the whole construction. In addition the top and the bottom

plate work as heat shield, i.e. prevent radiative losses of heat. The top plate is much thicker (0.5 cm) than the other plates because it is fixed to a vacuum tight metal plate which functions as closure of the glass tube. The coaxial interfaces for the thermocouple and the electronic contacts are inserted into the metal plate.
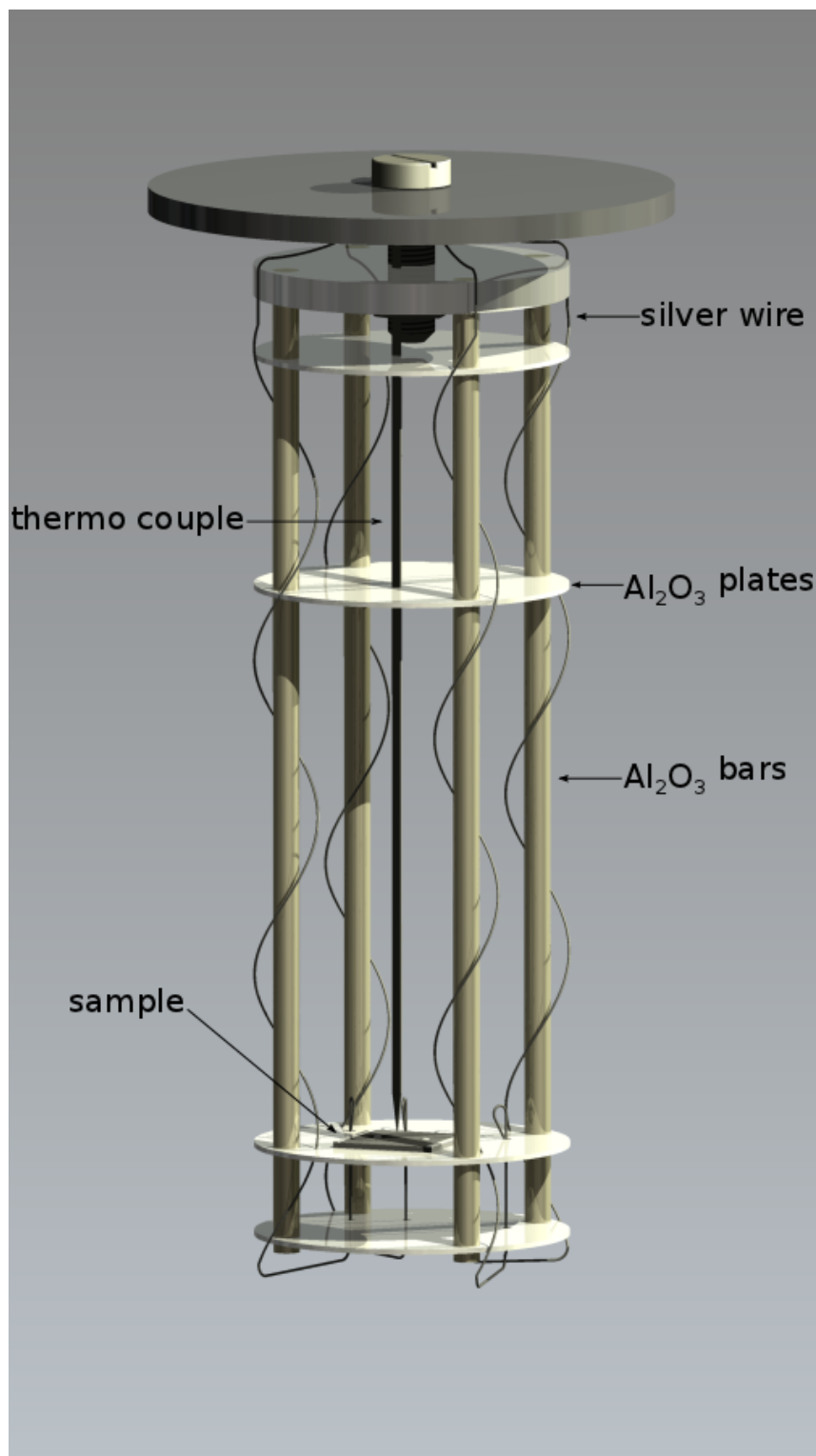
Figure 4.6: *Set up of the sample holder designed for high temperature resistivity measurements.*

A type-K thermocouple is located from the top plate along drill-holes inside the plates at a distance of 1 cm from the sample. Silver wires (diameter 0.05 cm) are installed from the top plate along the ceramic bars to provide current and voltage connections.

Finally, the sample lies on an Al_2O_3 plate in the middle of the sample holder which is located in the centre of the furnace.. To apply the four point method four contacts are made on the surface of the sample using silver paste. At the two outer contacts electric current is provided which forms a homogeneous electric field, and at the inner contacts a voltage drop is measured.

4.2.2 Transition Temperatures and Resistivity

The resistance measurement was performed from room temperature to 200°C. The temperature was increased continuously for 1 K/min to minimize the effect of an overshoot. The current between the outer contacts was hold constant at 0.0005 mA while the voltage between the inner contacts was measured. The temperature dependent resistivity diagram is shown in Figure 4.7.
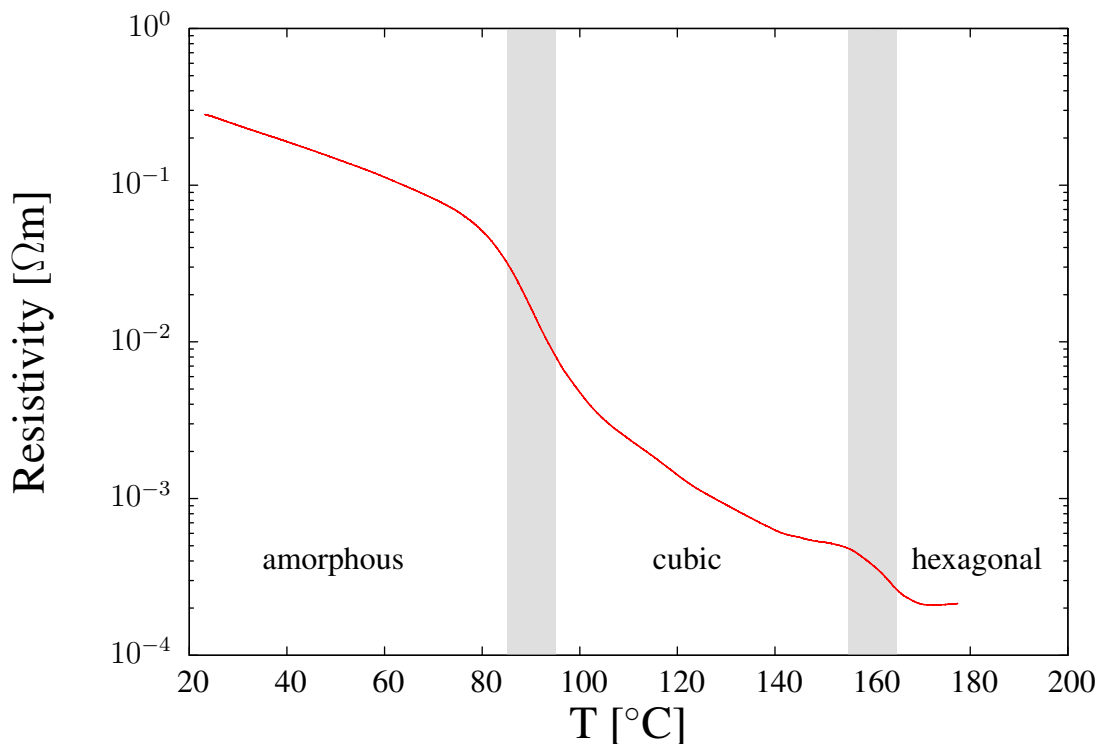
Figure 4.7: *Temperature dependent resistivity curve measured on SST. There are two drops of the resistivity at about 85° to 95°C and 155° to 165°C which indicate the phase changes from amorphous to cubic and from cubic to hexagonal, respectively.*

In order to get rid of instrumental artefacts, the graph was smoothed by a savitzky golay

filter which performed a local quadratic regression of every 5000 points. This procedure did not modify the general shape of the graph but supports to underline the main information. The resistivity ρ is determined by the measured resistance R using the formula:

$$\rho = R \cdot \frac{A}{d} \tag{4.2}$$

In this equation A represents the sample's cross-section as the product of its width and thickness and d is the distance between the two inner contacts. The resistivity of SST decreases by two to three orders of magnitude upon crystallization. For comparison, useful PCMs such as $GeSb_2Te_4$ and $Ge_2Sb_2Te_5$ show changes in the resistivity by four to five orders of magnitude [2].

The graph shows the general character of the resistance of a semiconductor with increasing temperature. In between there are two clear, but also quite broad resistance drops which are related to the phase transitions of SST. At 85° to 95°C the material switches from the amorphous state to the metastable cubic structure, and at 155° to 165°C the stable hexagonal structure is obtained. During cooling down the sample from 200°C, the resistance stays constant (not shown in the figure).

4.3 Resonant Ultrasound Spectroscopy

Resonant ultrasound spectroscopy (RUS) was used in order to determine the elastic constants of amorphous SST. This technique is based on the measurement of the acoustic resonant spectrum and the extraction of the elastic constants. The values for the elastic constants are compared with reference data for GST.

4.3.1 Experimental Set-Up

A challenge for RUS measurements of thin films lies in the preparation of the samples. The substrate must match the nearly perfect geometry of a parallelepiped with polished, parallel faces [21]. Additionally, a volume of 1 mm^3 is preferable with similar lengths in all three dimensions. To obtain reasonable results the film should have at least 1/1000 of the substrate's thickness.

The mounted sample is illustrated in Figure 4.8. The sample is carefully coupled and held lightly on opposite corners by transducer strips. Each strip consist of two metal layers whose overlap form a small capacitor (active area) sandwiching a piezoelectric material with a thickness of several micrometres. Thus the resonances of this piece occur at much higher frequencies

than typical sample resonances. The transducer strips are attached to insulating blocks, from which one of them can be adjusted in order to vary the space between the transducers for mounting or extracting the samples. Between the transducers there is a grounded copper shield with a hole at the position of the sample to minimize the electromagnetic cross talk between the transducers.
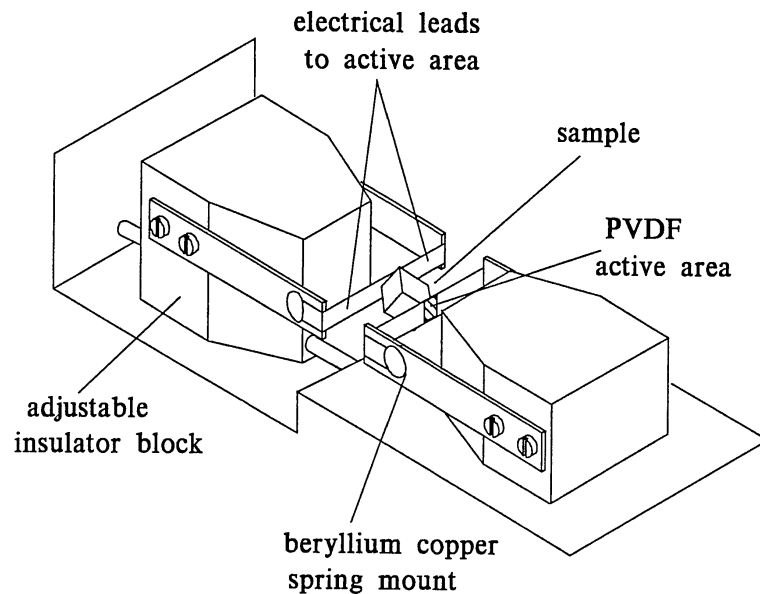
Figure 4.8: *Basic setup of the thin film RUS measurement. The sample is kept between to transducers consisting of metal stripes sandwiching a piezoelectric material. The transducers are fixed to insulating blocks from which one of them is adjustable to mount or unmount the sample[21].*

An AC voltage is applied to one transducer leading to an alternating electric field in the active area, and thus to a periodic contraction and expansion of the piezoelectric material. Through the attached corners an alternating stress with defined frequency is introduced into the sample. The receiving opposite transducer is strained by the motion of the sample inducing a voltage in the piezoelectric material which is recorded through the metal stripes.

The resonance spectrum is determined by the properties of the thin film and the substrate. To obtain the elastic constants of the film only, first a standard RUS measurement of the substrate is performed. Then the film is deposited on the substrate and the sample is remeasured (see Figure 4.9). In this procedure all substrate properties have to stay constant in order to minimize errors in the data analysis. The presence of the film leads to a frequency shift in the resonance spectrum, from which the elastic constants and thus the speed of sound of the film are calculated.
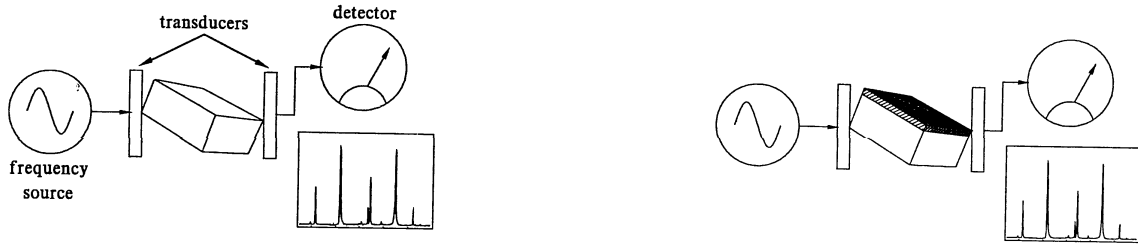
Figure 4.9: *Schematic drawing of the principle of RUS. An acoustic wave pulse is introduced and detected by transducers. First the substrate only is measured (left picture), then the substrate with the thin film on top (right picture). This leads to a shift of the peaks of the resonant spectrum [21].*

4.3.2 Experimental Results

RUS was performed on a 540 nm amorphous film of SST deposited on a 1 mm^3 cubic GaAs substrate. The resonance spectra of the substrate (blue curve) and the substrate with the film on top (red curve) are shown in Figure 4.10. The voltage amplitude of the detecting transducer is plotted against the ultrasound frequency.
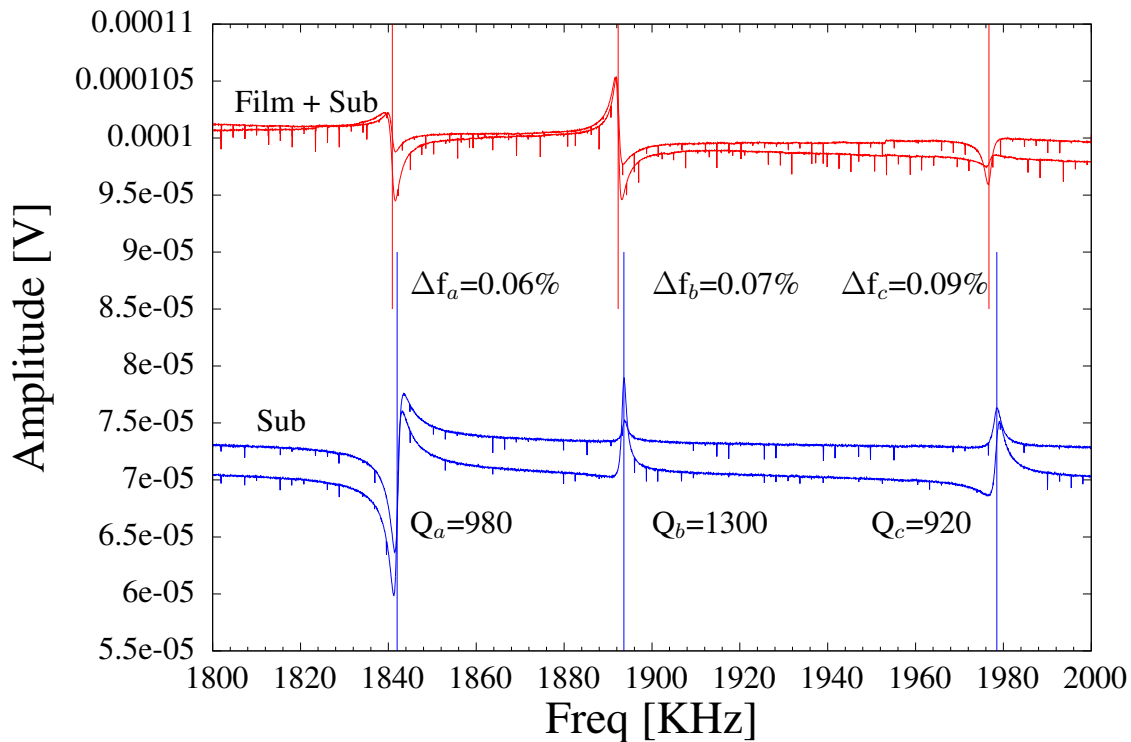
Figure 4.10: *Resonance spectra for the substrate and for the substrate with film. There is a small shift of the peaks to lower frequencies in the range of 0.1%. Q indicates the quality factors of the substrate's resonances.*

Due to the presence of the film the resonance peaks are shifted to lower frequencies. The

frequency shift is tiny in the range of 0.1% which is due to to the small thickness of the film. Every peak has been fitted by a Lorentzian profile in order to determine its position precisely. The quality factor Q of a resonance is related to the energy loss over one period, and is defined for small losses as the position of the peak f_0 divided by its FWHM. For reasonable results Q should be larger than 1000 which is given for the three substrate peaks shown in Figure 4.10.

The elastic constants were refined using a Levenberg-Marquardt minimization based on Equation 2.45. For the cubic GaAs substrate the elastic constants were calculated to $c_{11}^{sub} = 118$ GPa, $c_{12}^{sub} = 54$ GPa and $c_{44}^{sub} = 5.9$ GPa. The elastic constants of the substrate with the film on top is calculated considering a bilayer system. With these information the elastic constants of the film are obtained and listed is Table 4.3. Since no comparable RUS measurements have been performed yet on thin films on phase change materials, our obtained elastic constants are compared to those of GST determined by Brillouin light scattering [27].

	$c_{11}[GPa]$	c_{44} [GPa]
SnSb$_2$Te$_4$	112(1)	57.3(5)
GeSb$_2$Te$_4$	31(2)	9.8(5)

Table 4.3: *Elastic constants of the substrate and of the film only determined by RUS measurements.*

The comparison between SST and GST shows three to six times larger elastic constants for our measurements. This, of course, leads to a much too large speed of sound of 2350 m/s for the amorphous phase of SST. Different reasons may contribute to this deviation:

The substrate could have changed its shape between the measurements leading to an additional shift of the frequencies. Furthermore the film thickness was at the lower limit of 1/1000 with respect to the substrate thickness. Therefore the frequency shift is very small and is more sensible to systematic errors. Two additional problems which probably disturbed our measurements are the sample loading and the temperature control.

Everytime the sample is loaded between the transducers, its exact position is slightly different. Figure 4.11 shows the resonances for three different loadings by differing the tension between the transducers. The shape and position of the resonance shifts for several kHz just because of different loadings.

Another effect which can be a reason for our too large elastic constants is the temperature control. The position of the resonances strongly depends on the temperature which was not specially controlled in our measurements. Figure 4.12 shows that a temperature change of ten to twenty Kelvin causes a frequency shift of several kHz.
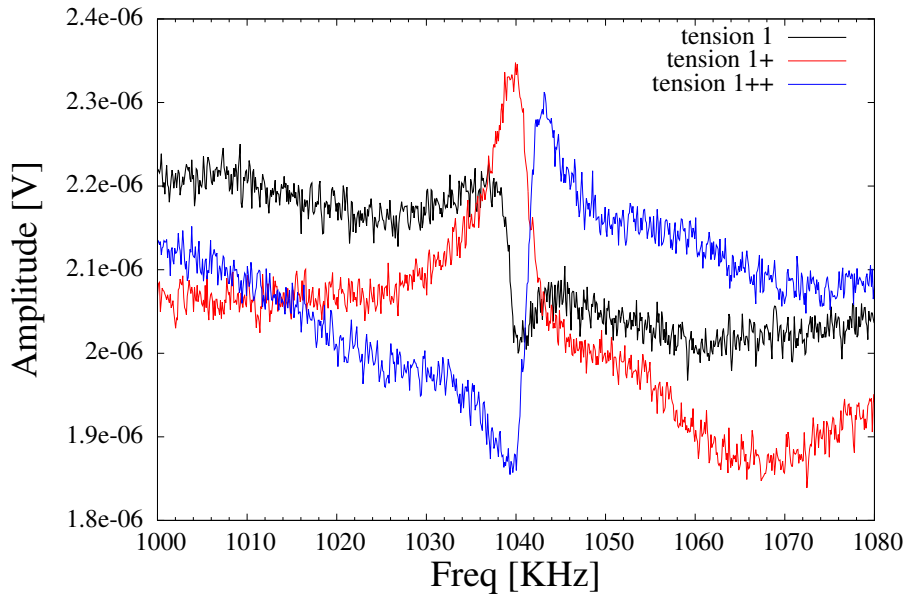
Figure 4.11: *Frequency shift due to different loadings of the samples. Different tension of the sample from the transducers leads to a shifting of the frequencies for several kHz.*
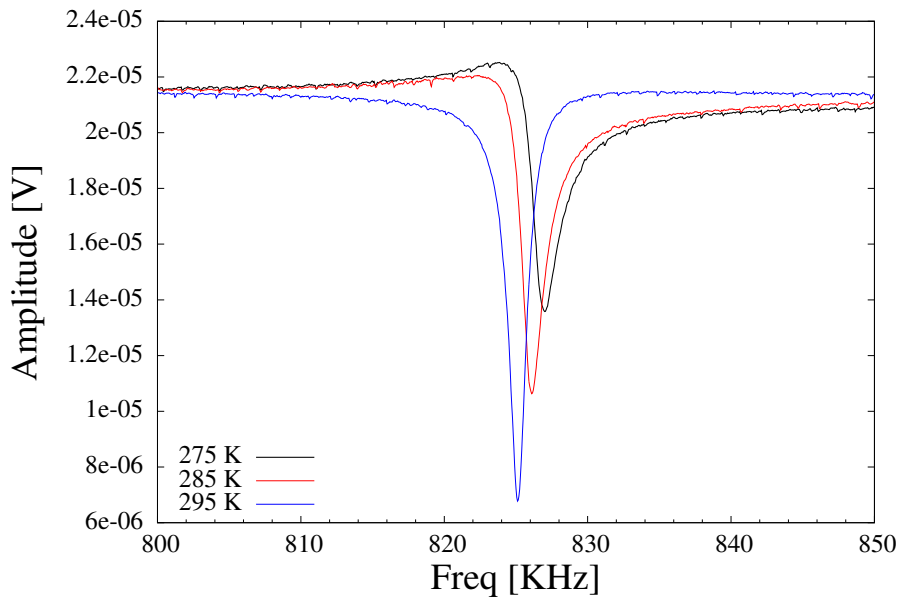
Figure 4.12: *Influence of the temperature control upon the resonances of the sample. A variation of ten to twenty Kelvin causes a shift of the frequencies for several kHz.*

Chapter 5

Nuclear Inelastic Scattering

In order to investigate the lattice dynamics of $SnSb_2Te_4$ (SST) nuclear inelastic scattering (NIS) was performed. This method can provide the element specific density of phonon states for all three elements both in the amorphous and in the two crystalline phases. Phonons are the main contribution for the thermal conductivity, which does not change as much in phase change materials between the amorphous and the crystalline phases (see Chapter 2.1) as would be expected for typical semiconductors. The currently established explanation describes a change from covalent to resonant bonding [8]. NIS is applied to investigate the density of phonon states (DPS) of all three phases in order to explain the microscopic processes that take place upon phase transition, and are compared with $GeSb_2Te_4$ (GST). SST is an isoelectronic substitution of GST by having access to the density of phonon states of ^{1}19Sn. Additionally extracted parameters such as force constants and mean square displacements give further information about the bonding strength.

5.1 Set-Up of the Beamline

Nuclear inelastic scattering sets strict requirements for the experimental set-up. Large x-ray energies between 10 and 80 keV, dependent on the isotope, with a resolution in the meV range is required to excite a nucleus resonantly. Therefore a special beamline with an adequate set-up is built to fulfil these conditions. The nuclear inelastic scattering measurements during this thesis work were performed at the beamlines ID18 and ID22N at the European Synchrotron Radiation Facility in Grenoble, France. A schematic sketch of the beamlines is shown in Figure 5.1.

The synchrotron radiation beam passes through a compound reflective lens (CRL) for collimation. The CRL consists of a beryllium block with a regular order of cylindrically drilled holes. In a CRL the walls between these holes function as concave lenses. The incoming x-ray
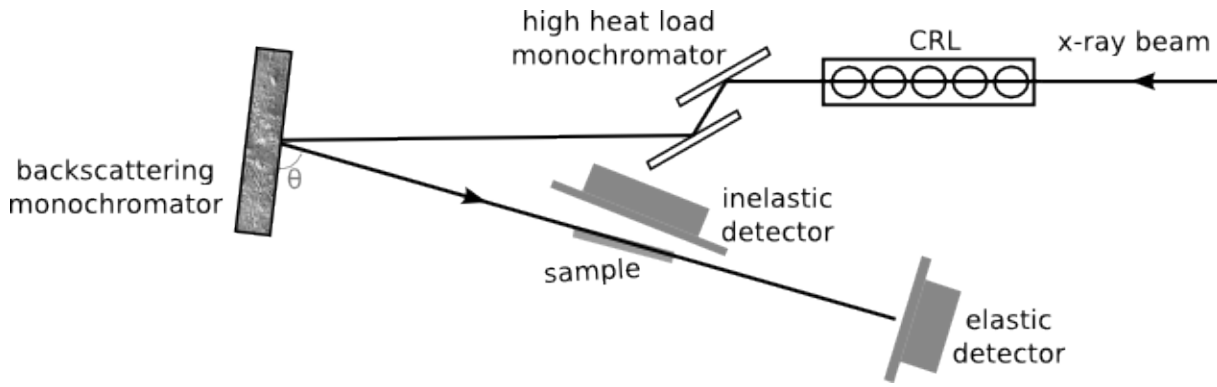
Figure 5.1: *Schematic set-up of the beamline applied for nuclear inelastic scattering. The synchrotron radiation beam is monochromatized to the eV range by the high heat load monochromator. The backscattering monochromator further reduces the bandwidth to meV by using a Bragg reflection $\Theta > 89.9°$. One detector is located close to the sample in order to cover a large angle of the inelastical signal. The second detector far away from the sample records the elastic peak.*

beam is collimated by these lenses as the reflection index for x-rays in this case is slightly under unity. The advantage of this arrangement is that the beam is slightly focussed at every single lens without having a large attenuation of the x-ray beam.

After the CRL the collimated beam is monochromatized into an eV bandwidth by a high heat load monochromator [18]. The high heat load monochromator consists of two independent Si crystals in which an asymmetric (1 1 1) Bragg reflections is used to reduce the bandwidth of the beam into the eV range at the expense of the flux which decreases by at least 20 %. The name of this monochromator comes from the high heat load which the first crystal has to face in the order of several kW/cm^2. Therefore the crystals have to be cryogenically cooled.

The beam is reflected at the backscattering monochromator which is made of a sapphire crystal of high purity [28]. A high order Bragg reflection is used to reduce the bandwidth of the beam to the sub-meV range. The spectral efficiencies for Sn, Sb and Te are listed in [28], but have been improved to, e.g., 35% for Te [29]. By varying the temperature of the crystal using liquid nitrogen and a heater with mK precision, the crystal expands or contracts, i.e. the lattice parameter changes, which offers the possibility to alter the reflection energy. Despite the high purity of the sapphire crystal some spots reveal a higher homogeneity than others. These spots are preferably used for the backscattering because they lead to a better reflectivity.

The sample is fixed to a copper block cut with an inclination of 1 mm/5 mm with respect to the beam. This angle leads to a better illumination of the sample. The sample is cooled in a cryostat and is covered by an aluminized mylar cap which works as thermal insulator. Before the beam is reflected by the backscattering monochromator it already passes through a window that is a few millimetres above the sample. The scattering angle, Θ, at the sapphire crystal is > 89.9° [28].

Avalanche photo diodes (APDs) serve as detectors because they provide a high count rate capability (up to a few GHz), low noise (0.01 Hz), and a fast recovery time necessary for NIS measurements [14]. Based on the photo effect, charge carriers inside thin silicon wafers are accelerated and amplified by the formation of secondary charge carriers. The inelastic detector is located close to the sample to cover a large angle and to detect as much of the incoherent inelastic signal as possible. The elastic detector records the nuclear forward scattering. It measures the resolution function and is located far away (several meters) from the sample to reduce the detection of inelastically scattered photons.

Nuclear inelastic scattering is a time resolved experiment which is based on the pulse structure of the synchrotron beam. Between two pulses the delayed nuclear fluorescence is detected without the large prompt signal due to electronic scattering and fluorescence. By using a veto, the electronics is prepared with a start and stop mechanism which allows the delayed nuclear fluorescence photons from the sample to be detected while the prompt, not delayed, beam is not counted. Because the delay depends on the lifetime of the excited state and thus on the isotope, the delay has to be electronically adjusted for every material.

5.2 Experimental Conditions

NIS measurements on SST were performed for the three isotopes ^{119}Sn, ^{121}Sb and ^{125}Te with the resonance energies 23.871, 37.133 and 35.4919 keV, respectively [14]. The samples were measured at low temperatures of 20 to 30 K in order to reduce multiphonon contributions. A low multiphonon contribution is helpful to extract the single-phonon contribution more precisely as it is directly connected to the DPS (Equation 2.26). The multiphonon contribution depends on the Lamb-Mößbauer factor, f_{LM} (Equation 2.35), which is lowered with increasing temperature due to lattice vibrations.

The energy was varied in a typical range of ± 40 meV around the elastic peak. For every sample several spectra were recorded and added in order to improve the statistics.

5.3 Density of Phonon States

The inelastic phonon spectrum and the elastic contribution are measured simultaneously by the inelastic detector while the instrumental function is recorded by the elastic detector. A typical spectrum is shown in Figure 5.2 for the ^{121}Sb isotope in hexagonal SST. In this diagram the instrumental function is shown in red and the data points of the spectrum in black with the corresponding error bars. Several data sets have been recorded and summed up by using a

typical binning of 0.4 meV to gain an increase in statistics. The resolution function is shrunk to the elastic peak of the spectrum.
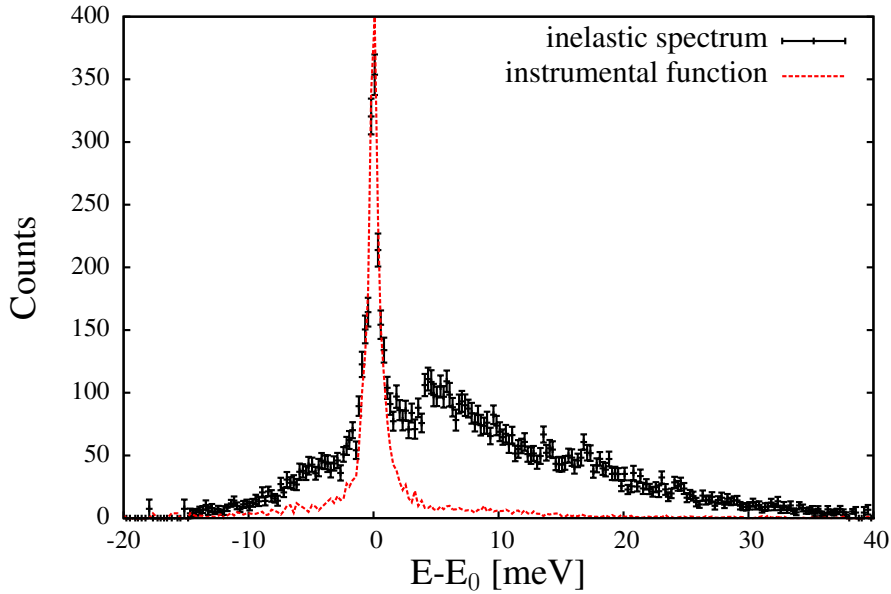
Figure 5.2: *Inelastic spectrum (black) and instrumental function (red) of hexagonal SST measured with the ^{121}Sb resonance.*

The spectrum has a large elastic peak at the resonance energy E_0. Positive values of the energy correspond to the creation and negative values the annihilation of phonons, respectively. For low temperatures (in our case 20 K) just a small amount of phonons are populated in the material, so that in the spectrum the phonon creation side is dominating. With increasing temperatures the spectrum becomes more symmetric with respect to the energy. The relation between annihilation and creation of phonons is given by the Bose-Einstein statistics which can be calculated from the spectrum:

$$\frac{I(E)}{I(-E)} = e^{\frac{E}{k_B T}} \tag{5.1}$$

In the latter equation $I(E)$ and $I(-E)$ indicate the intensities at the energies E and $-E$, respectively. The temperature of the sample during the experiment can thus be calculated precisely from the spectrum.

The single-phonon contribution is determined in two steps. First the elastic peak is subtracted from the measured spectrum. This normally leads to a strong oscillation in the region of the peak which would significantly perturb the DPS calculation. This non-physical part is smoothed, however, this region can not be trusted for the extraction of physical parameters. The second step consists of the separation of the single-phonon contribution from the multiphonon term and the deconvolution of the data from the instrumental function which is performed simultaneously

using a double Fourier transformation [19]. The extracted single-phonon contribution for the isotope [121]Sb in hexagonal SST is shown in Figure 5.3.
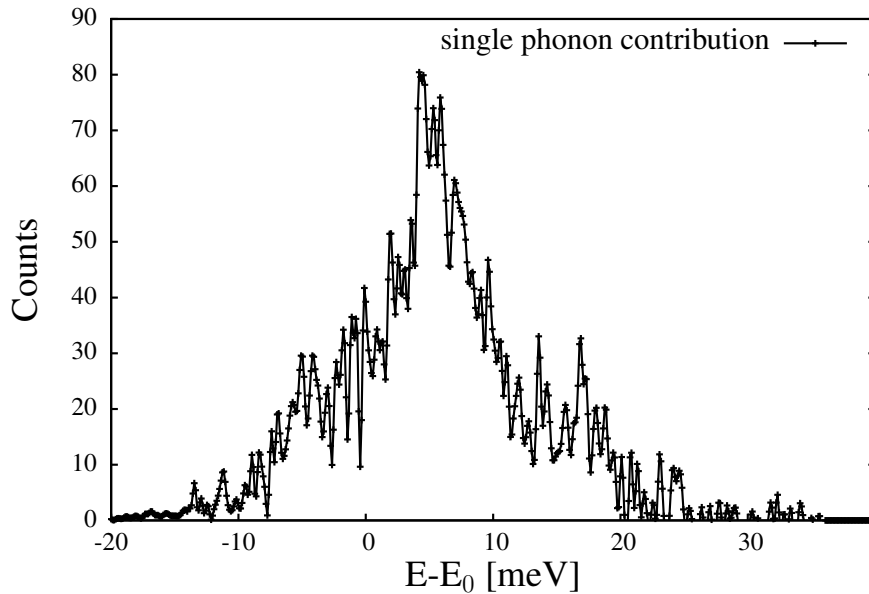
Figure 5.3: *The single-phonon contribution extracted from the inelastic spectrum.*

The DPS is calculated directly from the single-phonon contribution (Equation 2.26) by the software DOS [19]. Figure 5.4 shows the DPS separately for all three isotopes. The data are plotted up to an energy of 30 meV and were binned into 1 meV intervals.

At the first glance the DPS does not change significantly for Sb in the different phases. In Te the large peak at about 12 meV smears out to a broad area in the amorphous phase while in Sn the amorphous peak at around 6 meV flattens steadily upon crystallization. In general, the two crystalline phases show a similar shape for each isotope except of Sn. The reason for that is a broad and asymmetric instrumental function in the cubic phase which leads to difficulties with the subtraction of the central peak.

In the region of the low energy acoustic modes all three isotopes show a hardening upon crystallization which is an ordinary trend that is accompanied by an increase of the speed of sound (see Equation 2.20). On the other hand there is a softening of the high energy optical modes to lower energies for the Sb and Te isotopes. This effect, however, is not observed for Sn which means that there is no significant contribution from Sn to the phase change.

The same trend has already been observed for GST (see Figure 5.5). In Ref. [8] this softening was explained by a change from ordinary covalent to resonant bonding upon crystallization. Resonant bonding is accompanied by a large contribution of Peierls distortions and a strong softening of the transversal and longitudinal optical modes.

Figure 5.6 shows the partial and total DPS for the three phases of SST. In these diagrams the DPS of each isotope is multiplied by its relative abundance. The total DPS is calculated as
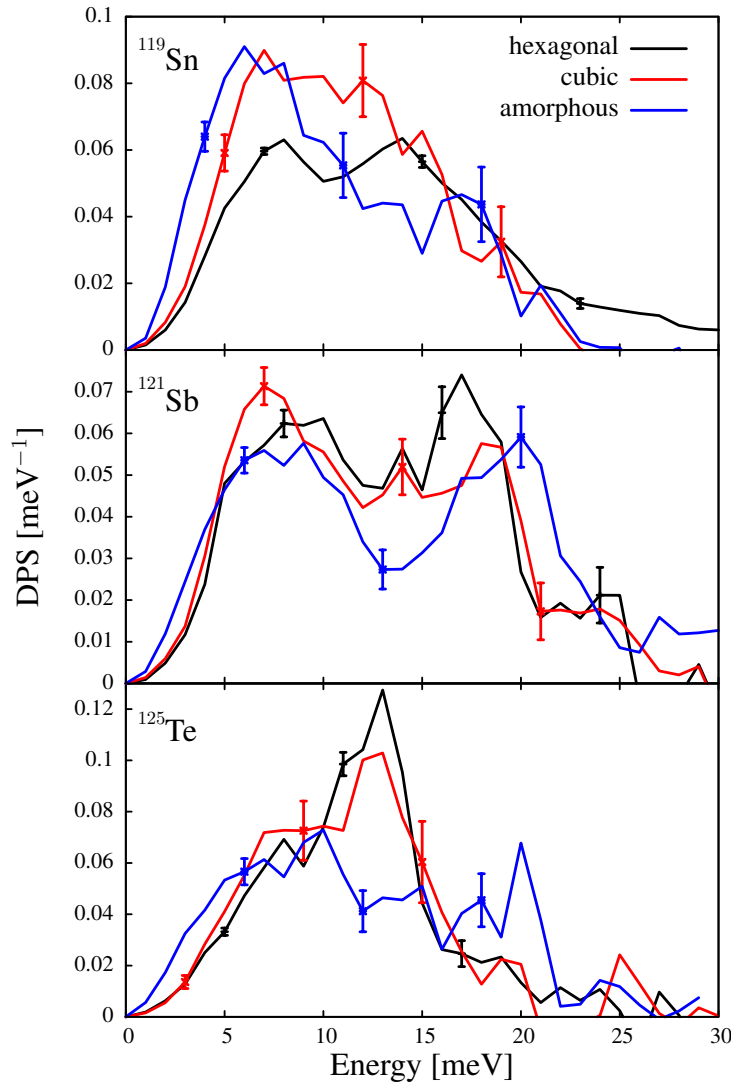
Figure 5.4: *The DPS for every isotope of SST. The hardening of the acoustic modes is observed in all three isotopes, however, the vibrational softening of the optical modes just occurs for Sb and Te.*

the sum of the three partial DPS. In the amorphous phase all isotopes contribute to a significant peak between 5 and 10 meV. This peak shifts to higher energies upon crystallization to 10 and 15 meV which is dominated by Te. The second peak in the amorphous phase around 20 meV softens upon crystallization. This effect is mainly due to the softening of the Te DPS, as the DPS of Sb and Sn do not change significantly.

All the DPS show the typical quadratic Debye behaviour below 2 meV (Equation 2.20). The pre-factor at very low energies is determined by the speed of sound inside the material, so that we should obtain the same Debye level for all three isotopes. In Figure 5.7 the DPS divided by E^2 and by the mass of the active isotope m_R in atomic mass units (amu) is plotted against the energy in the range of 0 to 20 meV. The Debye level should thus provide a constant level which
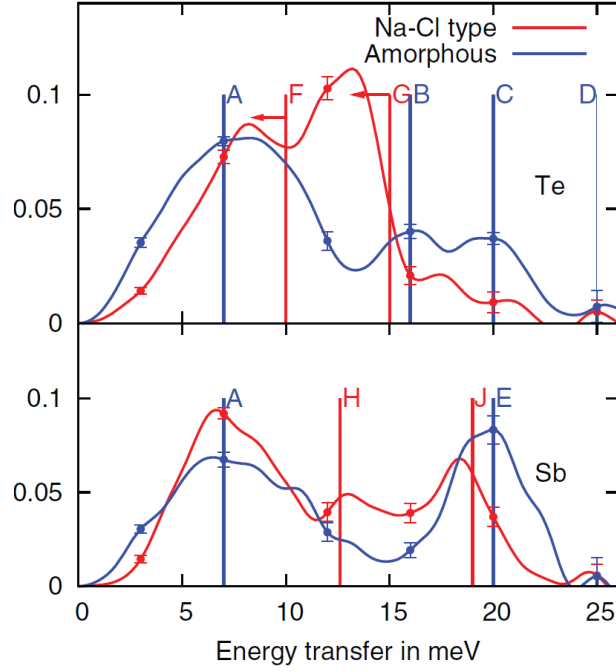
Figure 5.5: *DPS obtained for GST by nuclear inelastic scattering [8]. It shows large similarities compared to the measured SST data.*

is indicated as dashed lines. The levels were determined in a region until 3 meV, however, for the amorphous and cubic samples, the Sn levels do not provide reasonable results. Probably this is a problem of the subtraction of the instrumental function, which significantly influences Debye level for low energies. For these two measurements a broadening of the instrumental function was observed.

The deviation of the Debye level was estimated by noise level in Figure 5.7. This relative error in the Debye level propagates to about 1/3 for the relative error in the speed of sound v which is given by:

$$\lim_{E \to 0} \frac{g(E)}{E^2 m_R} = \frac{1}{2\pi^2 \rho \hbar^3 v^3} \tag{5.2}$$

The density ρ for the amorphous phase was determined via reflectometry measurements, for the crystalline phases it was calculated theoretically. The results are presented in table 5.1.

	Amorphous	**Cubic**	**Hexagonal**
Density [g/cm^3]	5.82	6.32	6.42
Debye level [1/meV^3/amu]	$2.3 \cdot 10^{-5}$	$1.1 \cdot 10^{-5}$	$1.0 \cdot 10^{-5}$
Speed of sound [m/s]	1300(70)	1620(70)	1660(150)

Table 5.1: *Debye levels and speed of sound determined for every phase of SST. A large increase of the speed of sound is observed upon crystallization. In the cubic and the hexagonal phase similar values are obtained.*
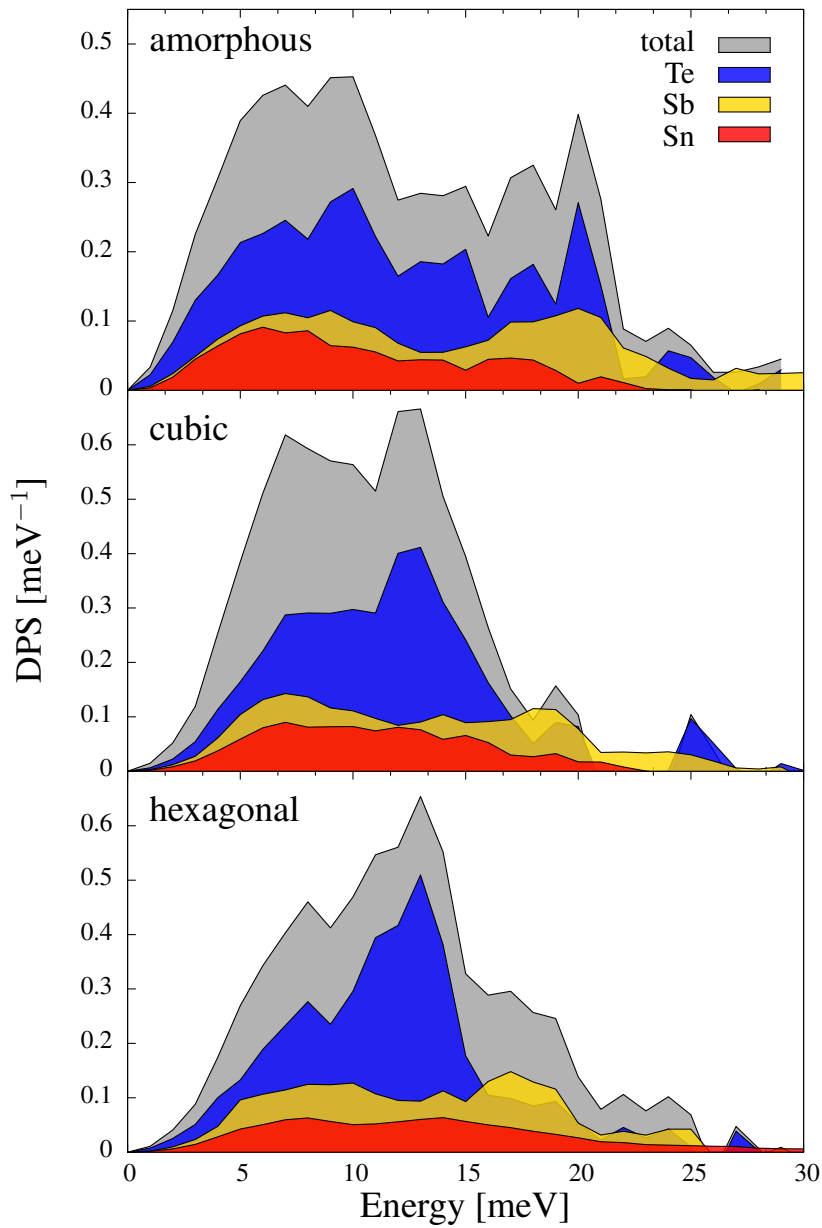
Figure 5.6: *Density of Phonon States extracted for all three phases of SST. Each isotope is multiplied by its atomic fraction in the SST compound, the total DPS is calculated by the sum of the partial DPS. The data are plotted up to an energy of 30 meV with a binning of 1 meV. The DPS of hexagonal Sn and the amorphous Sb converge to zero at about 40 meV which is not shown in the diagrams.*

The speed of sound shows an increase of about 25% upon crystallization and, as expected, the values for the crystalline phases are similar. The error bar in the speed of sound is about 70 m/s for the amorphous and the cubic phase, and about 150 m/s for the hexagonal phase.
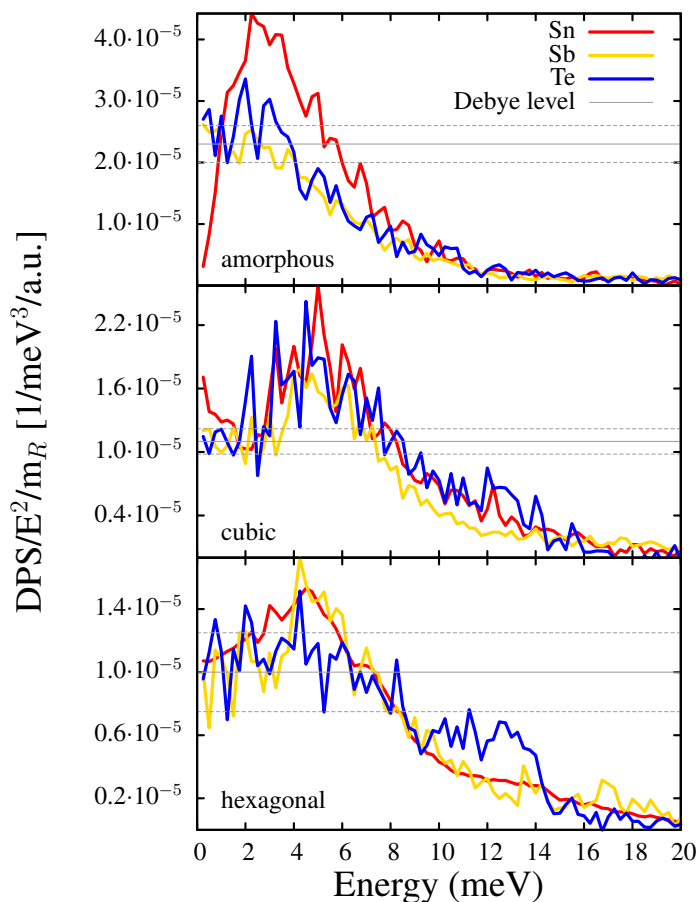
Figure 5.7: *Debye level for the amorphous, the cubic and the hexagonal sample. The Debye level is determined until around 3 meV and plotted with the error bar. For the amorphous and the cubic phase Sn was not considered in the determination of the Debye level.*

5.4 Thermodynamic Parameter

The results of the last chapter are used to calculate some material specific parameters. For the calculation of these parameters, the DPS and the spectrum were cut at energies below 30 meV because above these values oscillations appear which are an artefact from the subtraction process. The force constant F can be derived both from the DPS and from the inelastic spectrum (Equations 2.31 and 2.34). The comparison of both values provides the possibility to check the data evaluation process and to give an estimation for the deviation. Furthermore the Debye temperature is obtained using Equation 2.37. The results are summarized in table 5.2.

The force constant is obtained from the second moment of the DPS, thus it is dominated by the high energy optical phonons. Because of the vibrational softening which was observed in Chapter 5.3, the force constants for Sb and Te are expected to decrease upon crystallization. This is due to a weaker resonant bonding in the crystalline phases with respect to the covalent

	Amorphous			Cubic			Hexagonal		
	Sn	Sb	Te	Sn	Sb	Te	Sn	Sb	Te
F [N/m]	58	113	85	63	91	73	66	92	73
θ_D [K]	114	144	125	146	158	156	156	169	158

Table 5.2: *Force constant and Debye temperature obtained from NIS measurements. The force constant for Sb and Te increases upon crystallization for 14 to 19% which supports the observation of vibrational softening. The standard deviation is estimated to 2 N/m. The Debye temperature increases constantly upon crystallization.*

bonding in the amorphous state. The force constant decreases upon crystallization in the case of Te by about 14% whereas the values for the cubic and the hexagonal phase are similar. The Sb force constant decreases by 19% from the amorphous to the crystalline phases. These numbers verify the vibrational softening which has been investigated for GST [8]. In the case of Sn, however, this trend is not observed in the DPS which is also expressed by the force constant which increases slightly by 12% upon crystallization.

A constant increase of the Debye temperatures for all three isotopes supports the observation of a hardening of the low energy modes as presented on Chapter 5.3. Every phase shows the largest Debye temperature for Sb, followed by Te and Sn. The values of the Debye temperature are similar to those of GST obtained by NIS measurements [30]. The average Debye temperatures are calculated with respect to their relative abundance and result to 130(30), 160(10) and 160(20) K for the amorphous, cubic and hexagonal phase, respectively. The speed of sound is obtained using Equation 2.38 and is shown in table 5.3 in comparison to the corresponding values of GST. The GST speed of sound was calculated from elastic constants measured via Brillouin light scattering [27] and the error bar was calculated using propagation of uncertainty.

Speed of sound [m/s]	Amorphous	Cubic	Hexagonal
$SnSb_2Te_4$	1400(300)	1640(100)	1700(150)
$GeSb_2Te_4$	1000(30)	1230(30)	1340(50)

Table 5.3: *The speed of sound of SST compared to GST obtained by NIS measurements. Both show a significant increase upon crystallization, the values of the cubic and the hexagonal phase are similar. Within their deviations the speed of sound of SST is consistent with the values which were calculated in Chapter 5.3.*

The speed of sound of SST shows an increase by about 20% upon crystallization while the values for both crystalline phases are very similar. These values are in range of the deviation of those obtained in Chapter 5.3. GST shows the same trend upon crystallization, however, the SST values are 20 to 40% larger.

The Lamb Mößbauer factor f_{LM} is also obtained from the inelastic spectrum and from the

DPS using Equations 2.28 and 2.32, respectively. From the calculated values, the temperature dependence of f_{LM} is obtained by an harmonic approximation, in which the DPS does not change with temperature. The result is plotted in Figure 5.8. The crosses indicate the Lamb-Mößbauer factor measured by NIS during the experiment.
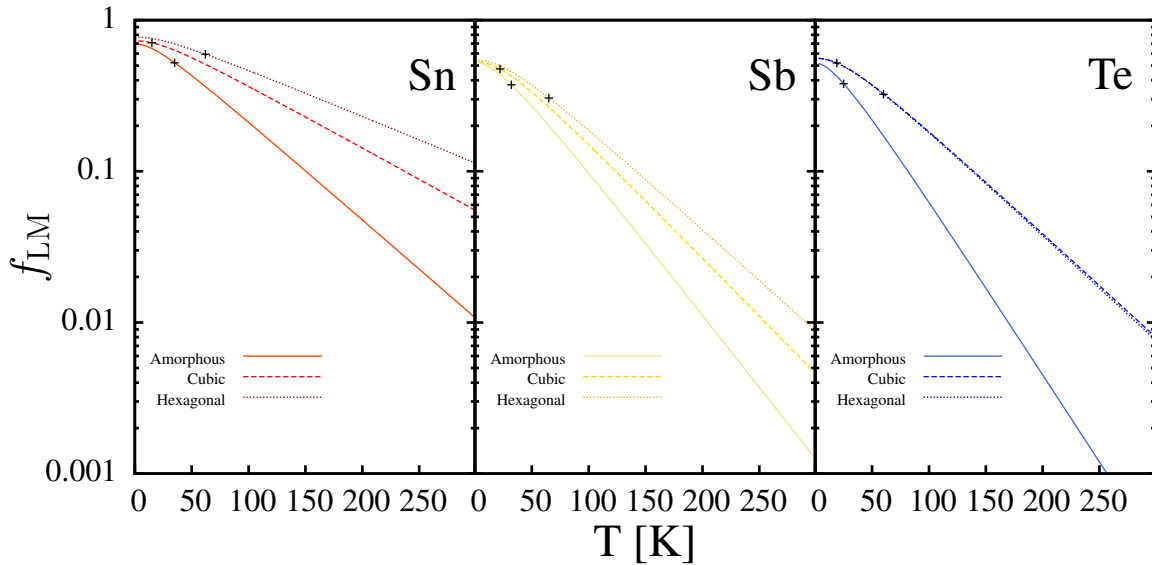
Figure 5.8: *Temperature dependence of the Lamb-Mößbauer factor. All f_{LM} drop by two to three orders of magnitude between 10 and 300 K. For Te the crystalline curves overlap.*

In all cases the measured values are below 0.6 with a deviation each of 0.01, which means that there is a large multiphonon contribution in the spectra which is difficult to subtract completely. Because the Lamb-Mößbauer factor is calculated from the minus-one moment of the DPS, it mainly depends on the acoustic phonons. Therefore the relatively large value which is obtained for cubic Sn is not reliable because there was a broad, asymmetric instrumental function which may distort the subtraction from the spectrum leading to unreliable data in the low energy part. For all three isotopes, the amorphous SST shows the lowest f_{LM} followed by the crystalline phases. Between 10 K and room temperature the Lamb-Mößbauer factors decrease by two to three orders of magnitude due to increasing lattice vibrations.

The mean square displacement $<x^2>$ is given by Equation 2.24 from the Lamb-Mößbauer factor. Table 5.4 shows the displacement at 25 K in comparison to values for GST [8]. The deviation of the displacement of SST was calculated by propagation of uncertainty to $5 \cdot 10^{-5}$ Å^2. The GST values have a deviation of $3 \cdot 10^{-5}$ Å^2.

The displacements of SST are in good agreement with the GST values. Both materials show a decrease up to 30% by switching from the amorphous to the cubic phase. The hexagonal phase

$<x^2>$ [10^{-3}Å^2]	Amorphous			Cubic			Hexagonal		
@ 25 K	Sn	Sb	Te	Sn	Sb	Te	Sn	Sb	Te
SnSb$_2$Te$_4$	3.63	2.47	3.00	2.69	2.19	2.17	2.16	2.03	2.19
GeSb$_2$Te$_4$	—-	2.33	2.51	—-	2.10	2.03	—-	—-	—-

Table 5.4: *Mean square displacements of SST, given in 10^{-3}Å^2, compared to reference values of GST [8]. The deviations of the SST and GST values are $5 \cdot 10^{-5}$ Å^2 and $3 \cdot 10^{-5}$ Å^2, respectively. There is a decrease of the displacement upon crystallization by 30% which is consistent with the GST values.*

for SST is similar with the cubic phase according to Sb and Te, however, the Sn value shows a further decrease from the cubic to the hexagonal phase.

Finally the atomic heat capacity C$_V$ in units of the Boltzmann constant was obtained from the DPS using Equations 2.36. Its temperature dependence is depicted in Figure 5.9. The total heat capacity is calculated by the sum of the partial values from the isotopes with respect to their relative abundance.
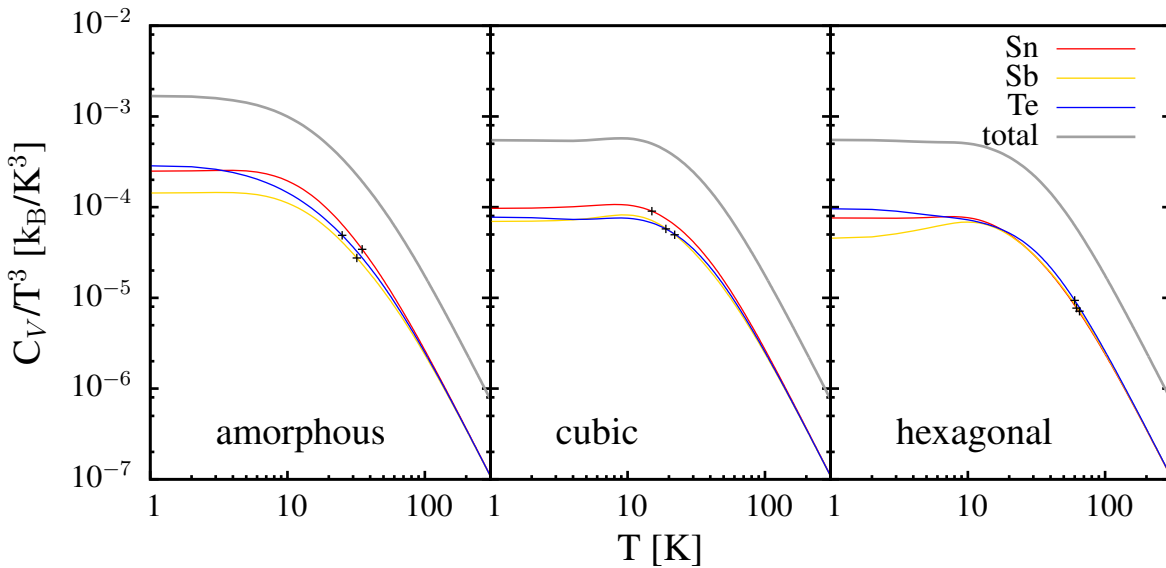
Figure 5.9: *Heat capacity at constant volume for the amorphous, cubic and hexagonal phase. The temperature dependence was calculated from the DPS in a harmonic approximation. The total heat capacity is the sum of the partial heat capacities with respect to their relative abundance.*

Chapter 6

Conclusion and Outlook

In this diploma thesis the structure, the temperature driven phase change and the lattice dynamics of the phase change material $SnSb_2Te_4$ (SST) is investigated. Substituting Sn by the isoelectronic Ge, one of the most studied phase change materials, $GeSb_2Te_4$ (GST), is formed. However, the lattice dynamics of Ge in GST are not well investigated yet. Thus, herein, using nuclear inelastic scattering measurements on isotropically enriched SST, we reveal the vibrational properties of ^{119}Sn and we give insights in understanding the phononic properties in this class of materials.

The feasibility of sample preparation using two different methods is described. Using the first method, based on vapour deposition, we are able to prepare a crystalline thin film without controlling the temperature of the substrate. On the other hand, magnetron sputtering with embedded temperature control is used resulting in an amorphous thin film.

Characterisation techniques, such as x-ray diffraction, electrical resistivity measurements and resonant ultrasound spectroscopy are performed in order to get access to physical properties. Using x-ray diffraction with subsequent profile matching, the phases of SST are clearly identified and the extracted lattice parameters (cubic: a = 6.165 Å, hexagonal: a = 4.252 Å, c = 42.625 Å) are 2 to 3% larger than in GST. Furthermore, diffraction measurements reveal that the annealing procedure used herein leads to crystallite sizes of about 100 Å in the cubic phase.

From the temperature dependent electrical resistivity measurement we identify broad phase transitions between 75° and 85°C (amorphous - cubic) and between 140° and 150°C (cubic - hexagonal).

Using resonant ultrasound spectroscopy the elastic constants of an amorphous SST film (540 nm on a GaAs substrate) have been extracted. However, c_{11} is three and c_{44} six times larger in comparison to corresponding GST values. This large difference is explained by minor issues in the sample preparation and in the experimental setup which will be improved in future measurements.

Our main focus is on nuclear inelastic scattering which gives access to the density of phonon states (DPS) and to thermodynamic parameters. One of these parameters, the speed of sound, was extracted both from the Debye level (E < 4 meV), as well as from the Debye temperature which is obtained from the entire DPS. The speed of sound indicates the expected acoustic hardening upon crystallization and results to 1350 (amorphous), 1640 (cubic) and 1680 m/s, which is, however, 400 m/s lower than in GST.

The unique softening of the ^{121}Sb and ^{125}Te optical modes in SST investigated by nuclear inelastic scattering measurements is also observed in GST and is supported by a decrease (17%) of the extracted force constants upon crystallization. However, this phenomenon is not observed for ^{119}Sn, which gives hints on understanding the change of bonding upon crystallization.

In summary, compared to GST, SST has similar electrical, structural as well as lattice dynamical properties observed in the DPS and in extracted parameters such as Debye temperatures and mean square displacements. However, the difference in the speed of sound is not yet clarified, but could possibly be investigated by Brillouin light scattering.

List of Figures

Bibliography

[1] S. Raoux and M. Wuttig. "Phase Change Material: Science and Applications". Springer (2009).

[2] S. Raoux. "Phase Change Materials". Annual Review of Materials Research, vol. 39 25–48 (2009). doi:10.1146/annurev-matsci-082908-145405.

[3] M. Wuttig and N. Yamada. "Phase-change materials for rewriteable data storage". Nature Materials, vol. 6(12) 1004–1004 (2007). doi:10.1038/nmat2077.

[4] P. B. Littlewood. "The Crystal-structure of Iv-vi Compounds .1. Classification and Description Rid B-7746-2008". Journal of Physics C-solid State Physics, vol. 13(26) 4855–4873 (1980). doi:10.1088/0022-3719/13/26/009.

[5] P. B. Littlewood. "The Crystal-structure of Iv-vi Compounds .2. A Microscopic Model For Cubic-rhombohedral Materials Rid B-7746-2008". Journal of Physics C-solid State Physics, vol. 13(26) 4875–4892 (1980). doi:10.1088/0022-3719/13/26/010.

[6] D. Lencer, M. Salinga, B. Grabowski, T. Hickel, J. Neugebauer and M. Wuttig. "A map for phase-change materials". Nature Materials, vol. 7(12) 972–977 (2008). doi:10.1038/nmat2330.

[7] K. Shportko, S. Kremers, M. Woda, D. Lencer, J. Robertson and M. Wuttig. "Resonant bonding in crystalline phase-change materials". Nature Materials, vol. 7(8) 653–658 (2008). doi:10.1038/nmat2226.

[8] T. Matsunaga, N. Yamada, R. Kojima, S. Shamoto, M. Sato, H. Tanida, T. Uruga, S. Kohara, M. Takata, P. Zalden, G. Bruns, I. Sergueev, H. C. Wille, R. P. Hermann and M. Wuttig. "Phase-Change Materials: Vibrational Softening upon Crystallization and Its Impact on Thermal Properties". Advanced Functional Materials, vol. 21(12) 2232–2239 (2011). doi:10.1002/adfm.201002274.

[9] H.-W. Wöltgens. "Combinatorial material synthesis applied to Ge-Sb-Te based phase-change materials". Ph.D. thesis (2003).

[10] M. Wuttig. "Phase-change materials: Towards a universal memory?" Nature Materials, vol. 4(4) 265–266 (2005). ISSN 1476-1122.

[11] G. Concas, T. M. De Pascale, L. Garbato, F. Ledda, F. Meloni, A. Rucci and M. Serra. "Electronic and Structural-properties of the Layered $Sn_1Sb_2Te_4$ Semiconductor: Abinito Total-energy and Mossbauer-spectroscopy Study". Journal of Physics and Chemistry of Solids, vol. 53(6) 791–796 (1992). doi:10.1016/0022-3697(92)90191-F.

[12] J. L. F. Da Silva, A. Walsh and H. Lee. "Insights into the structure of the stable and metastable $(GeTe)_m(Sb_2Te_3)_n$ compounds". Phys. Rev. B, vol. 78(22) 224111 (2008).

[13] W. Demtröder. "Experimentalphysik 3: Atome, Moleküle und Festkörper". Springer (2005). ISBN 9783540214731.

[14] R. Röhlsberger. "Nuclear Condensed Matter Physics with Synchrotron Radiation: Basic Principles, Methodology and Applications". Springer (2004).

[15] T. Brückel, G. Heger, D. Richter, G. Roth and R. Zorn. "Neutron Scattering - Laboratory Course", vol. 15 (2010).

[16] H. Ibach and H. Lüth. "Festkörperphysik: Einführung in die Grundlagen". Springer (2008).

[17] Y. Chen and D. Yang. "Mössbauer effect in lattice dynamics: experimental techniques and applications". Wiley-VCH (2007). ISBN 9783527407125.

[18] R. Ruffer and A. I. Chumakov. "Nuclear inelastic scattering". Hyperfine Interactions, vol. 128(1-3) 255–272 (2000).

[19] V. G. Kohn and A. I. Chumakov. "DOS: Evaluation of phonon density of states from nuclear resonant inelastic absorption". Hyperfine Interactions, vol. 125(1-4) 205–221 (2000).

[20] R. P. Hermann, F. Grandjean and G. J. Long. "Einstein oscillators that impede thermal transport". American Journal of Physics, vol. 73(2) 110 (2005).

[21] J. R. Gladden. "Characterization of Thin Films and Novel Materials using Resonant Ultrasound Spectroscopy". Ph.D. thesis (2003).

[22] A. Migliori and J. Sarrao. "Resonant ultrasound spectroscopy: applications to physics, materials measurements, and nondestructive evaluation". Wiley (1997).

[23] C. Dellen. "Isoelektronische Substitution in AIV1 BV2 CVI4 Systemen. $Ge_1Sb_2Te_4$ - $Ge_1Bi_2Te_4$ - $Sn_1Sb_2Te_4$" (2010).

[24] "Guinier Imaging Plate Camera G670 - Instruction Manual".

[25] A. Guinier. "X-ray Diffraction" (1963).

[26] T. Matsunaga and N. Yamada. "Structural investigation of $Ge_1Sb_2Te_4$: A high-speed phase-change material". Physical Review B, vol. 69(10) 104–111 (2004). doi:10.1103/PhysRevB.69.104111.

[27] T. Blachowicz, M. G. Beghi, G. Güntherodt, B. Beschoten, H. Dieker and M. Wuttig. "Crystalline phases in the $Ge_1Sb_2Te_4$ alloy system: Phase transitions and elastic properties". Journal of Applied Physics, vol. 102(9) 093519 (2007). doi:10.1063/1.2809355.

[28] I. Sergueev, H.-C. Wille, R. P. Hermann, D. Bessas, Y. V. Shvyd'ko, M. Zajac and R. Rüffer. "meV monochromatization of hard X-rays with a sapphire backscattering monochromator". Journal of Synchrotron Radiation, vol. 18(5) 802–810 (2011). doi:10.1107/S090904951102485X.

[29] "http://www.esrf.eu/news/spotlight/spotlight130/index_html/".

[30] "Private communication with Dr. Ilya Sergeev".

Acknowledgements

At this point I would like to thank all people who supported me very kindly during the year of my diploma thesis. I really enjoyed being a part of the institute and I want to thank all colleagues for a great year with an excellent atmosphere. Especially I want to mention the following persons:

At first, my very special gratitude goes to my supervisor Dr. Raphaël P. Hermann who provided me a place in his group. He gave me the opportunity to work at this very interesting topic. I further thank him for his advise and support, and especially for his patience in the last year.

I thank Prof. Dr. Matthias Wuttig for the acceptance of the co-supervision of my diploma thesis at the RWTH Aachen.

I also would like to thank Prof. Dr. Thomas Brückel for bringing me close to solid state physics during many interesting lectures and for giving me the possibility of writing my diploma thesis in his institute.

My special thanks go to Dimitrios Bessas who has always been a large support for me with his great ideas and his constant guidance through this work. I also appreciated sharing the night shifts with him during beamtimes at the ESRF.

I further thank Dr. Ilya Sergeev who has been a great local contact at ESRF. I thank him for his help and support during and outside of beamtimes.

Further thanks go to the rest of my group, especially Anne and Benedikt who did not stop giving answers to the many questions I asked them.

I thank Artur for his help with respect to software problems and general questions about physics, and Frank for his support with respect to mechanical problems.

Many thanks also go to my office members Markus and Johannes, and to the people from the neighbouring offices who provided a pleasant and comfortable surrounding.

I thank the group of Prof. Wuttig at the RWTH Aachen for a very kind collaboration, especially Gunnar Bruns and Stephan Hermes for the help with the sample preparation, as well as Peter Zalden for being my "local contact".